OXFORD

Journal of Petrology, 2025, **66**, egaf083
https://doi.org/10.1093/petrology/egaf083
ADVANCE ACCESS PUBLICATION DATE 17 SEPTEMBER 2025
Original Manuscript

Coupled Diffusion and Stress in Garnet from Holsnøy, Norway: Implications for Mineral Replacement Reactions and the Timescales of Episodic Heating and Fluid Flow during Subduction

BENJAMIN L. HESS [1,2], JAY J. AGUE[1,3] and HÅKON AUSTRHEIM[4]

[1]Department of Earth and Planetary Sciences, Yale University, PO Box 208109, New Haven, CT 06520-8109, USA
[2]Department of Earth Sciences, University of Oxford, South Parks Road, Oxford OX1 3AN, UK
[3]Yale Peabody Museum of Natural History, Yale University, 170 Whitney Ave, New Haven, CT 06511-8902, USA
[4]Department of Geoscience, University of Oslo, PO Box 1047, Blindern, Oslo N-0316, Norway

*Corresponding author: Telephone: +44 1865 272000. E-mail: benjamin.hess@seh.ox.ac.uk
†Handling Editor: Prof. Joerg Hermann

Holsnøy, Norway, offers a world-class natural laboratory for studying the impact of fluid on subducting lower crust. Holsnøy is composed of dry, metastable lower crustal granulite that was infiltrated by fluids along shear zones and seismic fractures during subduction. The infiltration facilitated the localized growth of eclogite facies mineral assemblages along the fluid flow pathways. The duration of the eclogite facies metamorphism, however, remains uncertain. Previous garnet diffusion chronometry studies have estimated timescales ranging from hundreds of years to millions of years based on diffusional relaxation between metastable granulite facies garnet cores and eclogite facies garnet rims and fractures. The shorter timescales are inferred from extremely sharp Ca gradients across chemical contacts present in some garnets whereas the longer timescales are from wider Mg and Fe profiles present in all garnets. The different timescale estimates have led to divergent models for the region's tectonometamorphic evolution. Here we show that the sharp Ca contacts can be explained by diffusion-induced compositional stress. As Ca is significantly larger than Mg and Fe, its movement strains the crystal lattice and generates stress that limits the relaxation of sharp chemical contacts. When compositional stress is accounted for, the sharp contacts yield timescales that are consistent with the wider Mg and Fe diffusion profiles. We determine that eclogite facies conditions (670–700 °C, 1.5–2.2 GPa) lasted a maximum of c. 300 kyr. The relatively short duration of eclogite facies conditions requires that multiple transient heating events were superimposed on a longer ($>10^6$ yr) overall timescale of metamorphism. Granulite facies garnet cores are surrounded by multiple generations of eclogite facies rims formed by interface-coupled dissolution–reprecipitation (ICDR) reactions. The garnet rims indicate two rapid, regional-scale fluid pulses and additional smaller, more localized pulses. The fluid pulses may be linked to episodes of seismic moment release as well as transient heating via exothermic hydration reactions and/or shear deformation. Our model results predict up to 400 MPa of differential stress at the garnet core–rim contacts, consistent with observed eclogite facies microfractures that extend into relic granulite facies garnet cores. The microfractures indicate that ICDR was aided by compositional stress: diffusion ahead of the reaction front generated stress and fracturing that created porosity for further ICDR. Thus, compositional stress can markedly impact both diffusion systematics and intracrystalline deformation. Together, these results show that despite their brevity, transient thermal, fluid flux, and/or baric episodes may exert the primary controls on the mineralogical and rheological development of subducted lithologies, in contrast to the long, slow burial and exhumation typically envisioned for regional metamorphism.

Key words: eclogite; garnet diffusion chronometry; intracrystalline stress; pulsed fluid flow; subduction

INTRODUCTION

Fluid flow in subduction zones is essential to the geochemical and rheological evolution of the lithosphere because fluids facilitate metamorphic reactions, affect rock strength, and transport volatiles. The island of Holsnøy, located in the Bergen Arcs in southwestern Norway, has been deemed a world-class natural laboratory for studying fluid–rock interactions in subducting continental crust (Fig. 1; Austrheim, 1987, 2013; Jamtveit *et al.*, 1990, 2000; Putnis *et al.*, 2017).

Studies from Holsnøy have revealed how infiltrating fluid reacted with subducting granulite facies continental crust to form eclogite facies shear zones that weakened the crust and facilitated later exhumation (e.g. Austrheim, 1987, 2013; Jamtveit *et al.*, 1990, 2019; Austrheim *et al.*, 1997; Jolivet *et al.*, 2005; Raimbourg *et al.*, 2005, 2007*b*; Putnis *et al.*, 2017; Petley-Ragan *et al.*, 2018; Zertani *et al.*, 2019; Bras *et al.*, 2021; Kaatz *et al.*, 2023). Studies documenting the reaction progress on Holsnøy elucidate the essential role that fluids play in catalyzing reactions in metastable mineral assemblages and enabling large-scale mass transport (e.g. Austrheim, 1987; Jamtveit *et al.*, 1990, 2000; Pollok *et al.*, 2008; Putnis & Austrheim, 2010; Putnis & John, 2010; Putnis *et al.*, 2017; Centrella, 2019; Bras *et al.*, 2021).

RECEIVED MARCH 12, 2025; **REVISED** SEPTEMBER 6, 2025; **ACCEPTED** SEPTEMBER 8, 2025

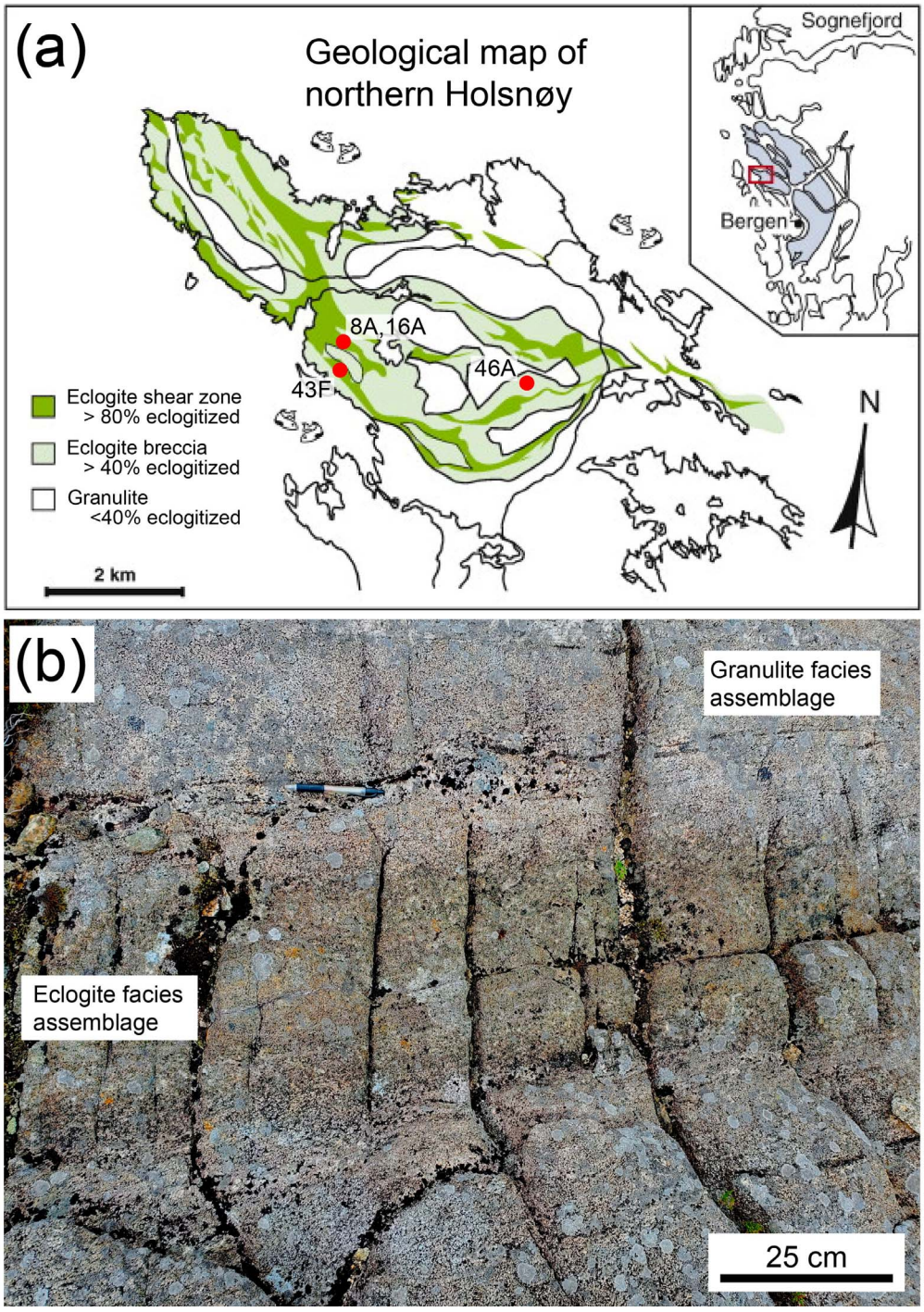

Fig. 1. Geological map of Holsnøy and example outcrop. (a) Map of Holsnøy, Norway with sample locations marked. Coordinates are provided in the Supplementary Information. Modified after Austrheim (2013). (b) Outcrop of an eclogite facies shear zone crosscutting an older granulite facies assemblage.

However, a fundamental uncertainty remains as to the duration of eclogite facies metamorphism and associated fluid flow on Holsnøy. Garnet diffusion chronometry and geochronology studies have provided inconsistent results: although some studies infer 10^5- to 10^7-yr timescales (Erambert & Austrheim, 1993; Boundy *et al.*, 1996; Perchuk, 2002; Glodny *et al.*, 2008), others have obtained 10^2- to 10^3-yr timescales or less (Camacho *et al.*, 2005; Raimbourg *et al.*, 2007*a*; Kaatz *et al.*, 2022).

Constraining this timescale is essential for relating the observed metamorphism to the tectonic processes of subduction and exhumation. If the duration of eclogite facies metamorphism was long (>10^6 yr), it is consistent with the timescales of slab motion with temperature being controlled by tectonic-scale thermal conduction. The metamorphic conditions can then be used to infer the long-term rheological strength and evolution of the subducting crust and to guide geochemical modeling (e.g. Jamtveit *et al.*, 1990, 2000, 2019; Raimbourg *et al.*, 2007*a*, 2007*b*; Putnis & Austrheim, 2010; Putnis *et al.*, 2017; Bras *et al.*, 2021; Kaatz *et al.*, 2021; Hess & Ague, 2024*b*).

In contrast, if eclogite facies metamorphism was short ($<10^6$ yr), it requires either extremely rapid exhumation or transient localized heating processes superimposed on the tectonic event such as shear heating, heat transport by fluid or melt, or exothermic reactions (e.g. Jamtveit *et al.*, 1990, 2021; Camacho *et al.*, 2005; Ague & Baxter, 2007; Raimbourg *et al.*, 2007*a*; Chu *et al.*, 2017). Such processes pose challenges to conventional geodynamic paradigms. Moreover, transient, localized heating events would imply that Holsnøy was potentially colder than is conventionally thought (e.g. the innovative 'cold-crust model' of Camacho *et al.*, 2005), changing our interpretation of the strength and evolution of the lower crust during subduction as well as the role that shear heating and fluids play in the thermal evolution of subduction zones.

Thus, it is imperative to constrain the timescale of eclogite facies metamorphism on Holsnøy. The aim of this study is to use garnet diffusion chronometry to harmonize the seemingly disparate past timescale results, and in doing so, provide new, consistent constraints on the timescales of eclogite facies metamorphism and the related fluid flow.

The diffusional relaxation of distinct chemical zones in minerals such as garnet can be used to estimate timescales of subduction zone processes (e.g. Faryad & Chakraborty, 2005; Chu *et al.*, 2017; Schwarzenbach *et al.*, 2021; Chen & Chu, 2024; Peillod *et al.*, 2025). Garnet is one of the best minerals for diffusion chronometry given its high symmetry and experimentally constrained diffusion rates (e.g. Chakraborty & Ganguly, 1992; Ganguly *et al.*, 1998; Carlson, 2006; Vielzeuf *et al.*, 2007; Chu & Ague, 2015; Chen & Chu, 2024).

However, one long-standing uncertainty is the role of stress in diffusion. The grossular end-member has a molar volume up to 10% larger than the other garnet end-members, and therefore, diffusion in garnet may generate considerable intracrystalline stresses. It has been proposed that diffusion-induced, or compositional, stress can impact the chemical evolution of crystalline solids such as minerals (e.g. Larché & Cahn, 1982; Baumgartner *et al.*, 2010; Neusser *et al.*, 2012; Chu *et al.*, 2017; Zhong *et al.*, 2017; Beyer & Chakraborty, 2021; Abart *et al.*, 2022; Hess & Ague, 2023, 2024*a*). Recent work shows that compositional stresses can prevent the relaxation of sharp chemical contacts in garnet, potentially changing the timescales estimated from diffusion chronometry by orders of magnitude (Hess & Ague, 2024*a*). In this study, we incorporate compositional stress into our modeling and find that it exerted strong controls on the diffusion systematics.

GEOLOGICAL SETTING: HOLSNØY, NORWAY

Holsnøy, Norway, is part of the Lindås Nappe in the SW portion of the Bergen Arcs (Fig. 1a). The island comprises metastable anorthositic to gabbroic granulite facies metaigneous rocks that reacted with metamorphic fluids at eclogite facies conditions during subduction (Austrheim & Griffin, 1985; Austrheim, 1987, 2013; Jamtveit *et al.*, 1990). The igneous protolith was a Proterozoic anorthosite complex that was emplaced during the Grenvillian orogeny and subsequently metamorphosed at 800–900 °C and ~1.0 GPa during the Sveconorwegian Orogeny at c. 930 Ma (Austrheim, 1987; Jamtveit *et al.*, 1990; Boundy *et al.*, 1997; Bingen *et al.*, 2001). The resulting granulite assemblages comprise plagioclase, clinopyroxene, garnet, and orthopyroxene with accessory spinel and scapolite (e.g. Austrheim & Griffin, 1985; Austrheim, 1987, 2013; Andersen *et al.*, 1990; Erambert & Austrheim, 1993). Metasomatically zoned ultramafic pods are also locally observed (e.g. Griffin, 1972).

The granulite was subducted to 50–80 km depth at ~430 Ma during the Caledonian Orogeny at which point fluids infiltrated along shear zones, pseudotachylytes, fractures, and other conduits (Jamtveit *et al.*, 1990; Boundy *et al.*, 1992; Erambert & Austrheim, 1993; Glodny *et al.*, 2008; Pollok *et al.*, 2008; Bhowany *et al.*, 2018; Zhong *et al.*, 2019). The fluids reacted with the precursor granulite to form shear bands and vein selvages of eclogite facies assemblages ranging from centimeters to tens of meters in width (Austrheim, 1987; Jamtveit *et al.*, 1990; Boundy *et al.*, 1992). These assemblages are composed largely of garnet, omphacite, and clinozoisite and may also contain zoisite, kyanite, phengite, paragonite, quartz, and rutile, depending on the local rock and infiltrating fluid chemistry (Jamtveit *et al.*, 1990; Boundy *et al.*, 1992; Perchuk, 2002; Bhowany *et al.*, 2018).

Investigations of garnet chemistry and zoning have led to different interpretations for eclogite facies metamorphism and the associated timescale. Erambert & Austrheim (1993) and Perchuk (2002) estimated that eclogite facies metamorphism lasted 1–4 and 0.8 Myr, respectively, based on Fe–Mg interdiffusion between relic granulite facies garnet cores and crosscutting eclogite facies cracks. In contrast, Raimbourg *et al.* (2007*a*) found sharp changes in Ca over a few micrometers at contacts between granulite garnet cores and eclogite facies garnet rims. The sharp contacts implied a much shorter 140- to 32 000-yr timescale. Thus, previous garnet diffusion chronometry studies have interpreted durations of eclogite facies conditions that differ by as much as five orders of magnitude. We will argue that accounting for compositional stress unifies these seemingly contradictory observations.

ANALYTICAL METHODS: IMAGING AND ELECTRON-PROBE MICROANALYSIS

A Leitz Sm-Lux-Pol petrographic microscope was used to identify garnets with vertical core–rim contacts for chemical analysis by adjusting the focus from the surface to the base of the thin section. Choosing vertical contacts allows the true sharpness of the chemical change between garnet cores and rims to be evaluated, facilitating an accurate measure of diffusional relaxation (e.g. Chu *et al.*, 2017; Hess & Ague, 2024*a*).

Backscatter electron (BSE) imaging, quantitative chemical profiles, and chemical maps were collected using the JEOL JXA-8530F field-emission gun electron-probe microanalysis (EPMA) at Yale University employing a focused beam, wavelength-dispersive spectrometers, linear off-peak background corrections, natural and synthetic standards, and $\phi(\rho z)$ matrix corrections.

Chemical profiles were collected with a 100 nA beam current and a 15 kV accelerating voltage for profiles with a 5–10 μm step size, and a 10 kV accelerating voltage for profiles with 1 μm step size. The 10 kV accelerating voltage facilitates a smaller activation volume with a diameter of ~0.8–1.5 μm, thus providing high spatial resolution (Ague *et al.*, 2012; Fournelle *et al.*, 2016). Uncertainties on plotted mole fractions are ±2σ sample SDs based on the measured Poisson counting statistics and reproducibility for each element (Hess *et al.*, 2025*a*). Mapping was done at 300 nA and 15 kV for larger maps (Figs 2a–d and 3) and 10 kV for smaller, higher resolution maps (Figs 2e–g and 4f).

SAMPLE DESCRIPTIONS AND TEXTURAL INTERPRETATIONS

Sample descriptions

We examine garnets from four eclogite facies samples that vary in bulk chemistry and deformation intensity (Table 1; Fig. S1).

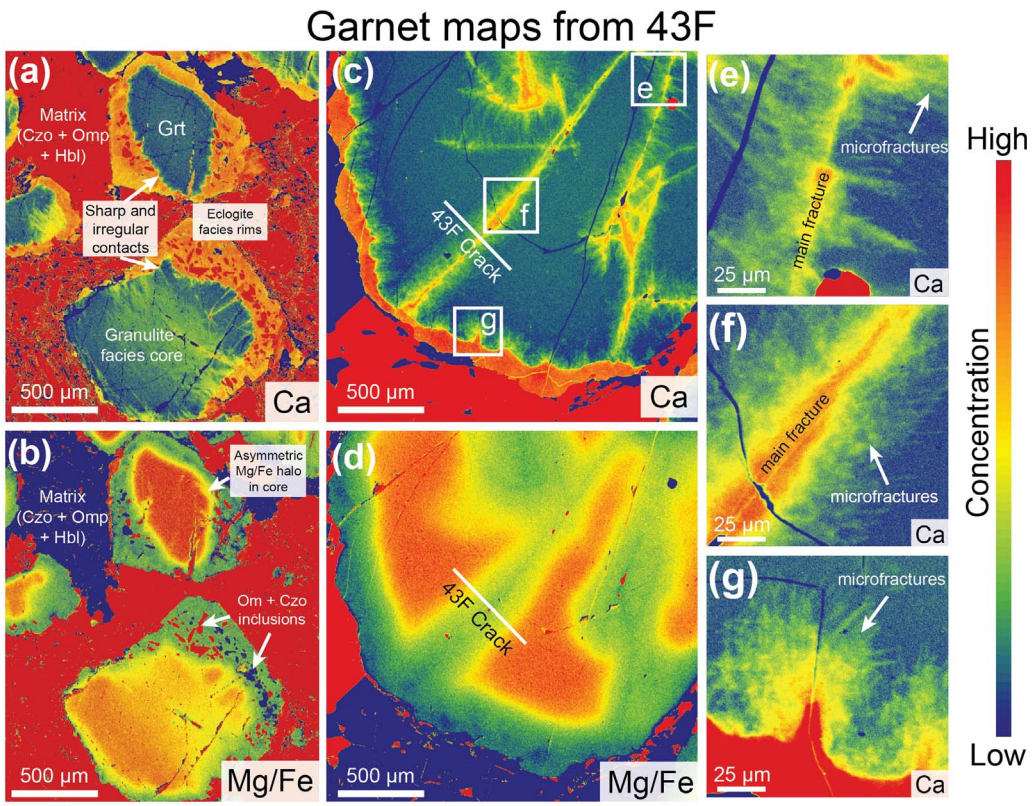

Fig. 2. Garnet (Grt) chemical maps for sample 43F. (a–g) Ca and Mg/Fe maps revealing garnet with distinct cores and rims. The matrix contains clinozoisite (Czo) (or zoisite) + omphacite (Omp) ± hornblende (Hbl), with lesser amounts of micas, kyanite, quartz, and rutile. Mineral abbreviations follow Warr (2021). The Ca maps show microfracture networks propagating from the core–rim boundaries into the garnet cores. The 43F Crack profile location is shown in parts (c) and (d). See text for further descriptions.

They have relic granulite facies cores and eclogite facies rims (Figs 2a and 3c) and are composed mostly of pyrope (Prp), almandine (Alm), and grossular (Grs) with very little spessartine (Sps). Samples 43F and 46A are from highly deformed meter-scale and dm-scale shear zones, respectively. Both samples display visible foliation (Fig. S1c and d), and their garnets have fractures that include other eclogite facies minerals such as omphacite and clinozoisite (Figs 2a, b and 3a, b). The main core–rim chemical change for sample 43F is between the mole fractions of Prp and Grs (X_{Prp} and X_{Grs}). For sample 46A it is between X_{Prp} and X_{Alm} (Table 1).

Samples 8A and 16A are eclogite facies meta-anorthosites in contact with ultramafic garnet-bearing hornblendite (8A) or clinopyroxenite (16A) pods (Fig. S1a and b). The samples are weakly foliated, and the garnets contain few, if any, peak eclogite facies cracks suggesting more limited brittle deformation than found in the highly deformed shear zones (Figs 3c, d and 4c–f). The garnet rims from the eclogite facies meta-anorthosite portions of samples 16A and 8A (Fig. S1a and b) have higher X_{Grs}, lower X_{Prp}, and similar X_{Alm} relative to the granulite facies garnet cores (Table 1). In contrast, garnet rims from the garnet-bearing hornblendite region of sample 8A have similar X_{Grs}, lower X_{Prp}, and higher X_{Alm} compared with the garnet cores.

Samples 8A, 16A, and 43F are spatially clustered, contain clinozoisite, and record oxygen fugacities that are 2.5–2.8 $\log_{10}$ units above the fayalite–magnetite–quartz buffer (ΔFMQ), consistent with other rocks from the region (e.g. Donohue & Essene, 2000; Boundy *et al.*, 2002). Sample 46A is distal to the other three, lacks clinozoisite, and has lower ΔFMQ of 0.5–0.8 (Table 1; Fig. 1). All samples have variable amounts of late amphibole-rich symplectite which, when present, has replacive textural relations with omphacite or eclogite facies garnet rims (e.g. Jamtveit *et al.*, 1990; Perchuk, 2002; Raimbourg *et al.*, 2007*a*; Bhowany *et al.*, 2018).

Chemical maps, BSE images, and profiles

Garnet chemical maps (Figs 2, 3, and 4f), BSE images (Fig. 4a–e), and quantitative chemical profiles (Figs 5 and 6) reveal complex zonation. Maps from samples 43F, 16A, and 8A display sharp, irregular Ca boundaries between the core and rim (Figs 2a, c, g, 3c, and 4f) with asymmetric Mg–Fe diffusion bands on the core side of the core–rim boundaries (Figs 2b, d and 3d). Notably, high-Ca 'wisps' or 'strands' propagate at a high angle from the core–rim boundaries into the cores. These are most apparent in 43F (Fig. 2c, e–g) but are also visible in the 46A and 8A Ca maps (Fig. 3a and c). Garnets from samples 8A, 16A, and 43F commonly preserve one or more relatively euhedral faces (Figs 2, 3c, d, and 4a, c–e) whereas the garnets from 46A generally have irregular rims (Figs 3a, b and 4b).

All granulite facies garnet cores have relatively homogeneous compositions whereas the eclogite facies garnet rims can exhibit considerable compositional variation (Figs 2, 3, and 4f). The chemical maps for 8A show complex but systematic variation in Ca, Mg, and Fe across the garnet rim (Fig. 3c and d). The variations align with contrast bands that are visible in the BSE images (Fig. 4c and d) and are marked on the chemical profiles (Fig. 6a and b). Sample 16A also reveals compositional heterogeneity as it preserves a local region of high Ca at the core–rim contact (Fig. 4f) that is also seen in the corresponding chemical profile (Fig. 6c). Notably, the high-Ca region does not appear in the other profile collected along the same garnet rim (Fig. 6d).

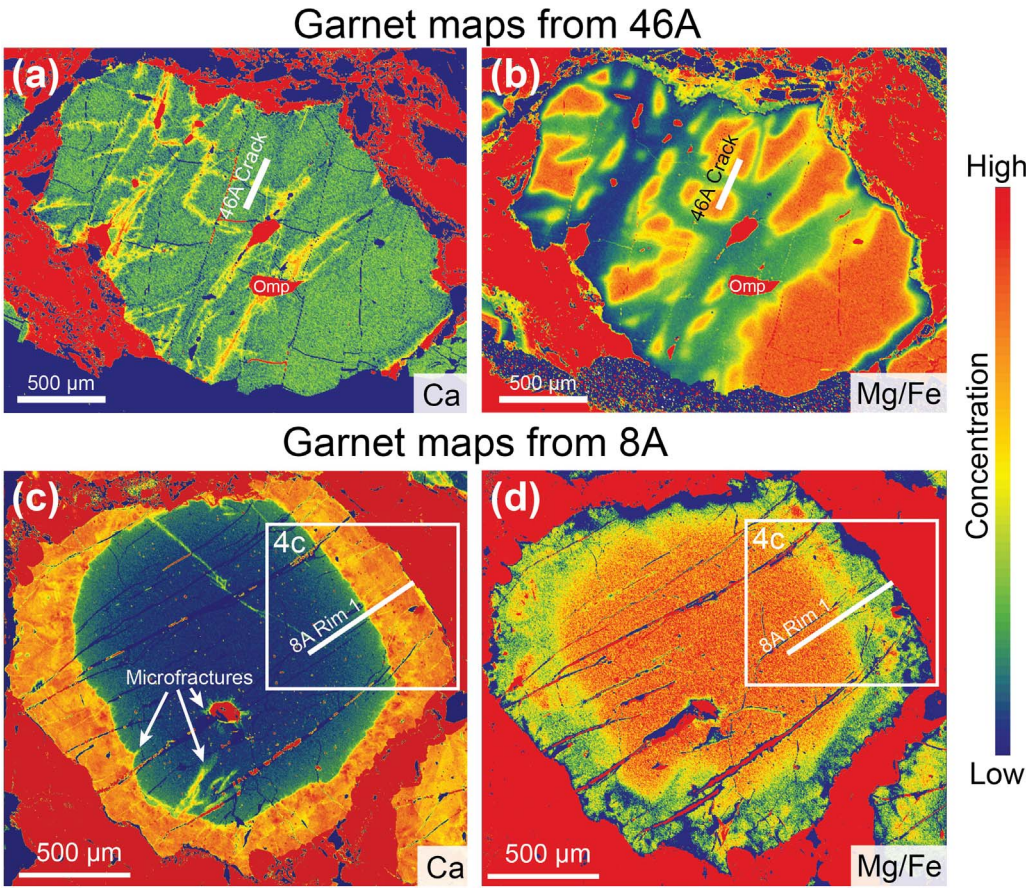

Fig. 3. Garnet chemical maps for samples 46A and 8A. (a, b) Ca and Mg/Fe maps from sample 46A. The garnets are fractured and have irregular rims. The location of 46A Crack profile is also shown. (c, d) Ca and Mg/Fe maps from sample 8A. Maps reveal small clusters of microfractures around the core–rim contact and chemical heterogeneities in the rim.

The qualitative observations from the chemical maps and BSE images are supported by quantitative chemical profiles that we separate into two categories. 'Crack' profiles run perpendicular to eclogite facies fractures that cut granulite facies cores (Fig. 5a and c). 'Rim' profiles run from eclogite facies rims inward toward granulite facies cores (Figs 5b, d and 6).

Crack profiles

The transected cracks contain eclogite facies garnet compositions that decay laterally into the granulite facies cores. The Alm and Prp components have relatively smooth composition changes whereas Grs exhibits significant heterogeneity (Fig. 5a and c). The extremely sharp variations in the X_{Grs} likely correspond to the high-Ca strands observed in the chemical maps (Figs 2c, e–g, and 3c). The 43F Crack profile reveals oscillations in X_{Grs} up to 0.01 mole fraction over single micrometer steps (Fig. 5a). The 46A Crack profile shows similar magnitude X_{Grs} heterogeneities but over the profile's larger 5 μm step size (Fig. 5c).

Rim profiles

The Rim profiles exhibit complex garnet rims with varying degrees of asymmetry across the core–rim contacts. The most symmetric transect is the 46A Rim profile, which has essentially equal length, smooth Alm and Prp curves across the core–rim contact at ~120 μm (Fig. 5d).

The remaining Rim profiles have varying degrees of asymmetry at core–rim contacts. The 8A Rim profile 2 and 16A Rim profile 1 have moderate asymmetry with the diffusion length scales on the rim sides being less than half the length scales on the core sides (Fig. 6b and c). Both profiles also have rims with multiple compositional plateaus separated by sharp composition changes that are most clearly marked by Grs. 16A Rim profile 1, for example, has an increase of 0.04 X_{Grs} at 40 μm and a sharp decrease of 0.06 X_{Grs} at the core–rim contact at 60 μm. These changes occur over a few micrometers in both cases (Fig. 6c).

The 43F Rim profile (Fig. 5b), 8A Rim profile 1 (Fig. 6a), and 16A Rim profile 2 (Fig. 6d) all have highly asymmetric contacts. The 43F Rim profile and 8A Rim profile 1 have relatively uniform rim compositions that abruptly drop by 0.05 X_{Grs} over ~2 and 6 μm at the core–rim contacts, respectively, and then all components decay smoothly into the garnet core compositions (Figs 5b and 6a). Similarly, 16A Rim profile 2 is essentially flat until the core–rim contact marked by a 0.02 X_{Grs} drop at 95 μm, after which the Alm and Prp components decay into the core composition (Fig. 6d). Notably, 16A Rim profiles 1 and 2 were collected along the same garnet rim (Fig. 4e), but profile 2 is both significantly more asymmetric than profile 1, and it does not contain the high Grs region measured in profile 1 (Figs 4f and 6c, d).

Textural interpretation

The garnet textures indicate a combination of intracrystalline volume diffusion, fracturing, and fluid-driven interface-coupled dissolution–reprecipitation (ICDR) reactions. We first provide background on ICDR and then describe how the observed textures relate to these processes.

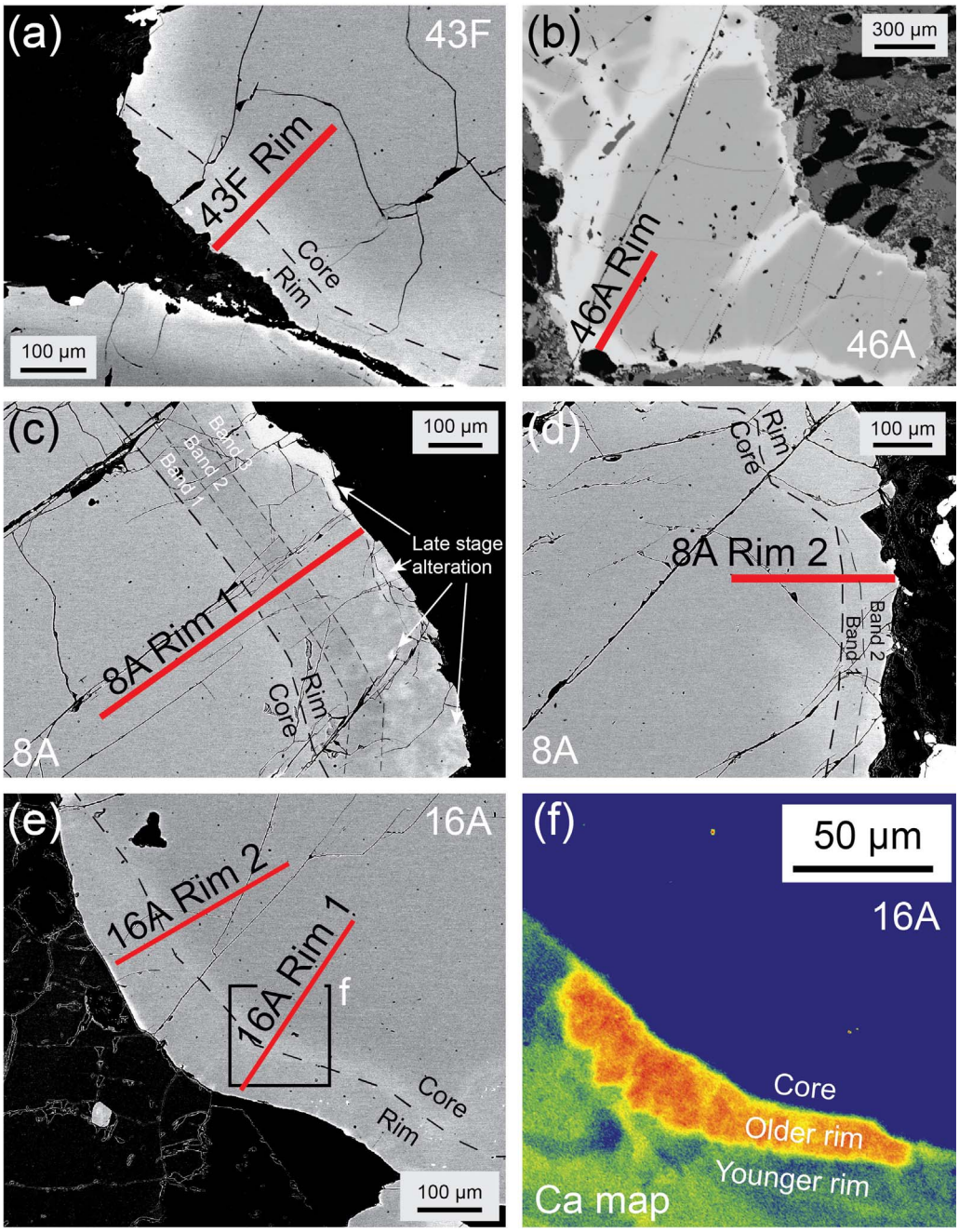

Fig. 4. Quantitative Rim profile locations. (a–e) High-contrast BSE images showing chemical profile locations. Black dashed lines mark the core–rim boundaries. In part (c) and (d) thin dashed lines demarcate distinct contrast bands in the garnet rim. Chemical maps for the region in part (c) are shown in Fig. 3c and d. (f) Ca map from boxed region in part (e) showing two distinct rim compositions.

Interface-coupled dissolution–reprecipitation reactions.

The ICDR mechanism operates in the presence of fluid or melt and replaces pre-existing minerals (e.g. Putnis, 2002, 2021; Putnis & Putnis, 2007; Ruiz-Agudo *et al.*, 2014; Altree-Williams *et al.*, 2015; Adegoke *et al.*, 2022; Gardner *et al.*, 2025). Infiltrating fluid dissolves minerals that are undersaturated with respect to the fluid, creating interfacial boundary layers on mineral interfaces that become supersaturated with respect to one or more stable phases that then precipitate.

The process depends on micro- or nanoporosity networks that form in product phase(s) via dissolution. The fluid-filled porosity network facilitates diffusive mass transport of reactants to and dissolved products away from the parent phase that drives an autocatalytic reaction that pseudomorphically and potentially epitaxially replaces minerals (e.g. Putnis, 2002, 2009, 2021; Geisler *et al.*, 2007; Putnis *et al.*, 2007; Putnis & John, 2010; Altree-Williams *et al.*, 2015; Centrella *et al.*, 2015). ICDR can proceed even if the molar volume of the product phase(s) exceeds the parent phase if dissolution rates outpace reprecipitation (e.g. Putnis & Putnis, 2007, 2022).

If the ICDR reaction only partially replaces a mineral, the resulting boundaries between parent and product phases are extremely sharp and typically irregularly shaped (e.g. Putnis *et al.*, 2007; Harlov *et al.*, 2011; Ague & Axler, 2016). Multiple episodes of fluid infiltration can create several generations of products (e.g. Ague & Axler, 2016). If the temperature is

Table 1: Garnet samples

Sample		8A	16A	43F	46A
Representative granulite facies garnet composition	X_{Alm}	0.45	0.41	0.45	0.28
	X_{Prp}	0.39	0.38	0.37	0.53
	X_{Grs}	0.15	0.20	0.17	0.18
	X_{Sps}	0.01	0.01	0.01	0.01
Representative eclogite facies garnet composition	X_{Alm}	0.45	0.43	0.50	0.47
	X_{Prp}	0.32	0.33	0.25	0.33
	X_{Grs}	0.22	0.23	0.24	0.19
	X_{Sps}	0.01	0.01	0.01	0.01
Oxygen fugacity (ΔFMQ)		+2.7	+2.8	+2.5	+0.5–0.8
Deformation intensity		Moderate	Moderate	High	High

Representative garnet core and rim compositions, oxygen fugacity (f_{O_2}), and deformation intensity are provided for each sample. The f_{O_2} values are given in $\log_{10}$ units relative to ΔFMQ. The reactions and mineral compositions used to calculate the f_{O_2} are given in Tables S1 and S2.

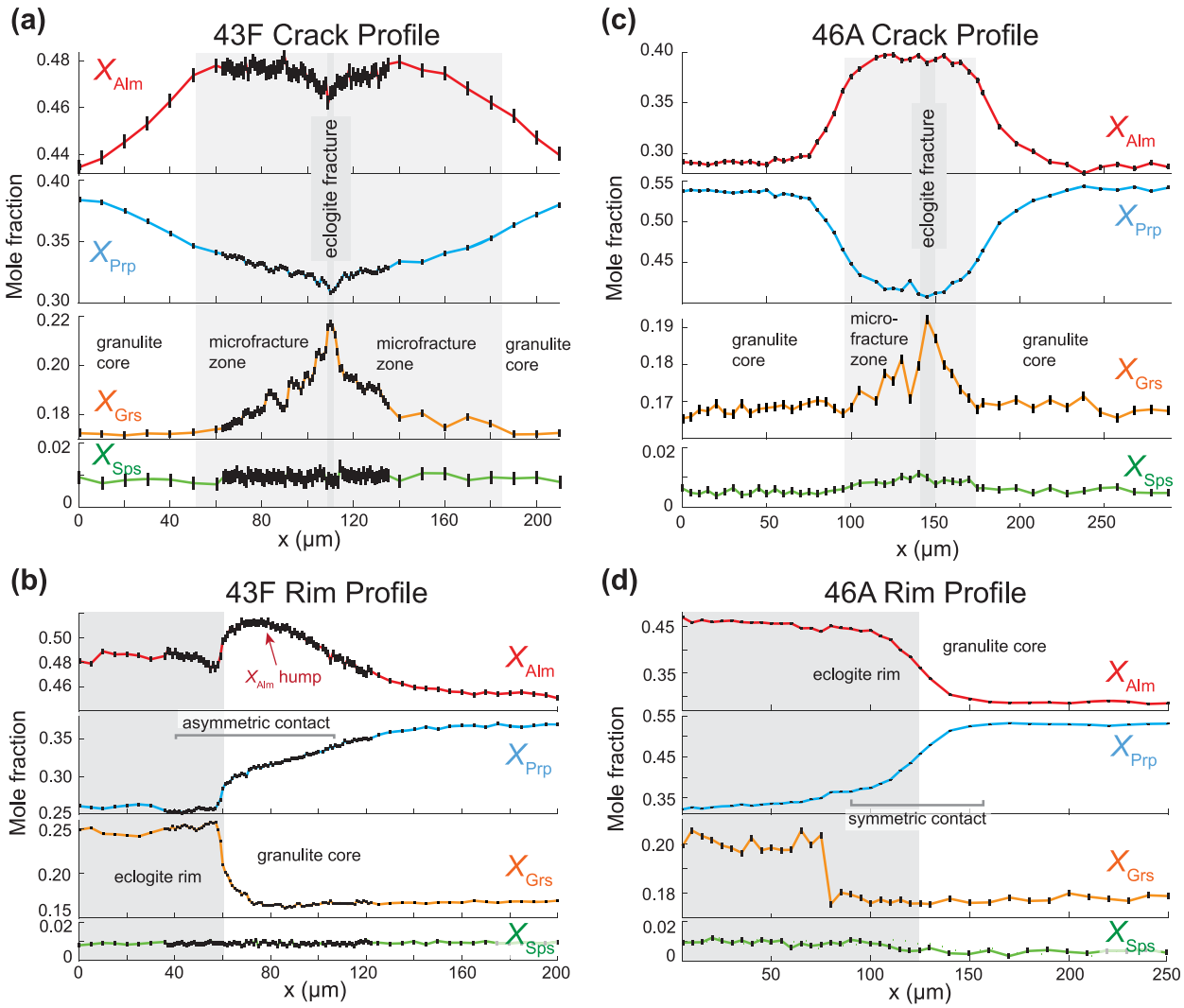

Fig. 5. Quantitative 43F Crack and Rim profiles (a, b) and 46A Crack and Rim profiles (c, d). In this and all following figures, black rectangles are measured data points with their heights representing two sigma precision uncertainty. The oscillating X_{Grs} values in (a) and (c) are interpreted to be due to microfractures (see text).

sufficiently high, subsequent diffusional relaxation can smooth the initially sharp chemical contact between parent and product phases (e.g. Pollok *et al.*, 2008). If multiple fluid infiltration episodes occur during prolonged diffusional relaxation, the diffusion profile may be partially or entirely overprinted (e.g. Plümper & Putnis, 2009; Ague & Axler, 2016). The partial replacement of diffusion profiles can create asymmetric chemical features.

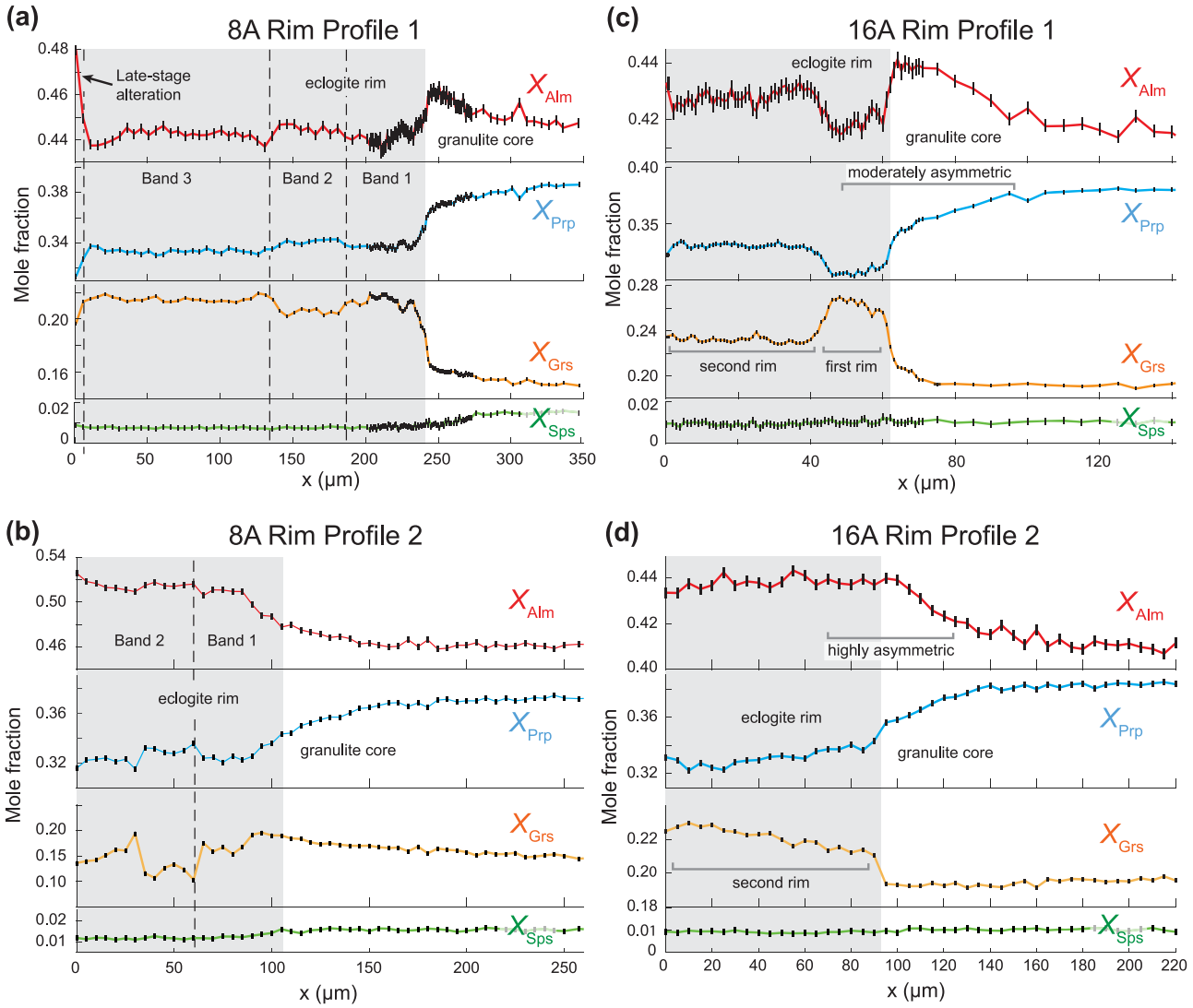

Fig. 6. Quantitative Rim profiles from samples 8A (a, b) and 16A (c, d). The bands denoted for 8A Rim profiles 1 and 2 correspond to contrast bands in associated BSE images (Fig. 4c–d). The 16A Rim profiles 1 and 2 were collected from the same garnet (Fig. 4e).

Garnet rims

It has been demonstrated that the eclogite facies garnet rim textures are indicative of ICDR (Pollok *et al.*, 2008), consistent with the well-established role of fluids in triggering eclogite facies metamorphism on Holsnøy (e.g. Austrheim, 1987, 2013; Jamtveit *et al.*, 1990, 2000; Erambert & Austrheim, 1993; Putnis *et al.*, 2021; Zertani *et al.*, 2022). The textures we observe corroborate these findings.

The core–rim boundaries are often irregular (Figs 2a, c, 3c, and 4), and the chemical profiles with large X_{Grs} changes have extremely sharp core–rim contacts (Figs 2a, 5b, and 6a, c). The core–rim contacts also exhibit varying degrees of asymmetry indicating multiple episodes of ICDR. Later ICDR events replace portions of the older garnet rim(s) that can partially erase developing diffusion profiles, creating asymmetry. The 16A Ca chemical map and Rim profiles 1 and 2 display the clearest evidence of multiple generations of garnet rims: an older, high-Ca rim has been partially replaced by a second, younger rim formed by a later ICDR event (Fig. 4f). The incomplete replacement created the moderately asymmetric chemical profile (Fig. 6c). Elsewhere along the same garnet rim, the older rim has been completely replaced, creating a highly asymmetric chemical profile (Fig. 6d).

Mineral inclusions in the eclogitic garnet rims and fractures have been previously interpreted as evidence of overgrowth (e.g. Raimbourg *et al.*, 2007*a*). However, it has been shown that there is a modal decrease in garnet for eclogite facies assemblages relative to the granulite precursor (Bhowany *et al.*, 2018; Bras *et al.*, 2021) with no significant change in garnet modes between inferred eclogite facies stages (Bhowany *et al.*, 2018). Consistently, neither the garnet rims nor the inclusions within the rims show evidence of growth textures (e.g. clear crystal faces or oscillatory zonation; Figs 2 and 3). Instead, porosity created by dissolution likely enabled eclogite facies minerals to nucleate and grow in the garnet rims with external components sourced by the fluid. There are numerous examples of inclusions formed by ICDR in the product phase that are absent from the parent phase (e.g. Tomaschek *et al.*, 2003; Harlov *et al.*, 2005, 2011; Geisler *et al.*, 2007; Putnis & Putnis, 2007; Engvik *et al.*, 2008, 2009; Rubatto *et al.*, 2008; Sung *et al.*, 2009).

Thus, the textures are consistent with the interpretation that the garnet rims formed via one or more ICDR replacement reactions (e.g. Pollok *et al.*, 2008). If any growth occurred, it has been completely overprinted by the ICDR accompanying eclogite facies fluid infiltration.

Garnet cracks and microfractures

The eclogite facies cracks crosscutting the granulite facies garnet cores (e.g. Fig. 2c) are interpreted to be contemporaneous with the onset of eclogite facies metamorphism (Austrheim, 1987; Jamtveit *et al.*, 1990, 2000; Erambert & Austrheim, 1993; Pollok *et al.*, 2008). The breakdown of strong granulite facies minerals reduced the rock strength, leading to elevated strain (e.g. Bras *et al.*, 2021, 2023; Kaatz *et al.*, 2021, 2022, 2023; Moulas *et al.*, 2022; Baïsset *et al.*, 2023; Filiberto *et al.*, 2025). Once the fractures formed, fluid propagated along them, leading to localized ICDR reactions that created the observed eclogite facies garnet assemblages within the fractures (Pollok *et al.*, 2008). After eclogite facies minerals grew to a sufficient size, the rock strength increased again, decreasing the strain rate (e.g. Bras *et al.*, 2021). Once sealed, the fractures were isolated from the additional fluid pulses seen in the garnet rims.

The garnet fractures are most prevalent in samples 43F and 46A, which are from well-developed shear zones with high strain (Figs 2, 3a, b, and 4a, b). In contrast, few eclogite facies fractures are observed in garnets from samples 8A and 16A, which are characterized by weaker foliations and more limited deformation (Figs 3c, d and 4c–f). However, some garnets in 8A and 16A have thin Fe-rich rims and/or fractures that crosscut peak eclogite facies garnet textures (e.g. the bright, Fe-rich rim in Fig. 4c). These late features are chemically distinct and formed during retrogression (e.g. Bhowany *et al.*, 2018), as confirmed by diffusion modeling below.

The main fractures have high-Ca strands that radiate from the fracture edges into the garnet cores. We interpret these to be micro- to nanofractures (Fig. 2c, e–g). The microfractured regions appear somewhat fuzzy because analytical convolution limits the resolution of sub-micrometer chemical variations (Ague *et al.*, 2012; Fournelle *et al.*, 2016). The observed Ca strands likely comprise dense networks of even smaller fractures, with the microfracture density decreasing with distance from the main fractures (Fig. 2c, e–g). Both the main fractures and the microfractures have healed, probably by fluids, as they are typically only visible due to the preserved compositional differences and remnant eclogite facies mineral inclusion trails (Fig. 2; Erambert & Austrheim, 1993; Perchuk, 2002; Raimbourg *et al.*, 2007*a*; Pollok *et al.*, 2008).

The microfracture networks propagate from the main fractures at high angles consistent with Mode 1 fracture tip propagation (Fig. 2c, e–g; Irwin, 1957). We hypothesize that in addition to external shear strain, the formation and propagation of the observed microfracture networks was aided by the stress and strain generated by chemical diffusion. As smaller Mg and Fe are replaced with larger Ca ions, the garnet structure becomes stressed, and when sufficient stress develops, it fractures. Diffusion-induced fracturing has been experimentally demonstrated for feldspar (Neusser *et al.*, 2012; Scheidl *et al.*, 2014). These fracture networks likely enhanced garnet chemical evolution by facilitating rapid vacancy- or fluid-mediated diffusion and ICDR along the microfractures that elevated the flux of material into the garnet by orders of magnitude compared to volume diffusion (e.g. Hart, 1957; Love, 1964; Brady, 1983; Hacker & Christie, 1991; Putnis & Putnis, 2007; Legros *et al.*, 2008; Harlov *et al.*, 2011; Piazolo *et al.*, 2016).

DIFFUSION MODELING

The following sections describe how the textural interpretations are incorporated into quantitative multicomponent diffusion modeling with compositional stress and ICDR.

Modeling approach

In what follows, 'diffusion' refers to slow, intracrystalline volume diffusion unless otherwise specified. There are also fast vacancy- and fluid-mediated diffusion pathways present in the garnets. As these mechanisms are orders of magnitude faster than typical intracrystalline volume diffusion (e.g. Hacker & Christie, 1991; Putnis & Putnis, 2007; Legros *et al.*, 2008; Piazolo *et al.*, 2016), we treat them as effectively instantaneous as described below.

Crack profiles

The Crack profiles record diffusion between the granulite garnet cores and the crosscutting eclogite facies fractures (Figs 2f and 5a). Figure 7 provides a conceptual model of how 1-D chemical profiles relate to 2-D garnet cross-sections. A chemical profile collected perpendicular to the main fracture will intersect microfractures that appear as spikes in composition. As diffusion occurs, the heterogeneities relax and produce the morphology of the Crack profiles (Fig. 5a).

The initial conditions oscillate between the compositions of the granulite facies garnet core and the eclogite facies garnet fractures (Fig. 7). Observed Grs spikes in the chemical profiles (Fig. 5a and c) are inferred to be locations of eclogite facies microfractures. The eclogite facies garnet composition is determined from the main fracture value whereas the granulite garnet composition is taken from parts of the garnet core unaffected by diffusion. Although the microfracture networks may have grown during diffusion via diffusion-induced stress (e.g. Scheidl *et al.*, 2014; Hess & Ague, 2024*a*), we conservatively assume that they were fully formed at the model start.

We use a mass balance approach to determine if the microfractures facilitated additional mass transfer into garnet cores. Mass balance is achieved when the concentration of each of the N end-members in the given garnet volume (C_i^{model}; mol m^{-3}) is equal to the observed garnet concentration (C_i^{obs}; mol m^{-3}). Numerically, the following set of conditions must be met:

$$\sum_{i=1}^{i=N}\left(\iiint C_i^{\mathrm{model}}dV = \iiint C_i^{\mathrm{obs}}dV\right) \tag{1}$$

If equation (1) is not satisfied, we allow the microfractures to act as material sources until the equality holds. We deem the most straightforward way to achieve this is by fixing the composition of microfractures (i.e. applying a Dirichlet boundary) until both sides of equation (1) are equal, and then allowing the microfracture compositions to relax. Numerically:

$$C(x) = C_e \text{ for } 0 < t < t_b \tag{2}$$

Equation (2) indicates that $C(x)$, representing the concentration at point x (the location of a microfracture), is equal to the eclogite facies garnet concentration, C_e, until time exceeds t_b. We adjust t_b in our models until equation (1) is satisfied. This procedure does not account for the effects of volume change, but the volume change due to diffusion or filling of microfractures would be small and have negligible impact (Hess & Ague, 2023). The precise garnet composition used in the microfractures does not meaningfully impact our timescale results, which are determined primarily from the width of the diffusion limbs.

Rim profiles

The Rim profiles record episodic ICDR reactions during prolonged diffusional relaxation. Figure 8 provides a conceptual model of how ICDR and diffusion operate together. Fluid infiltration forms

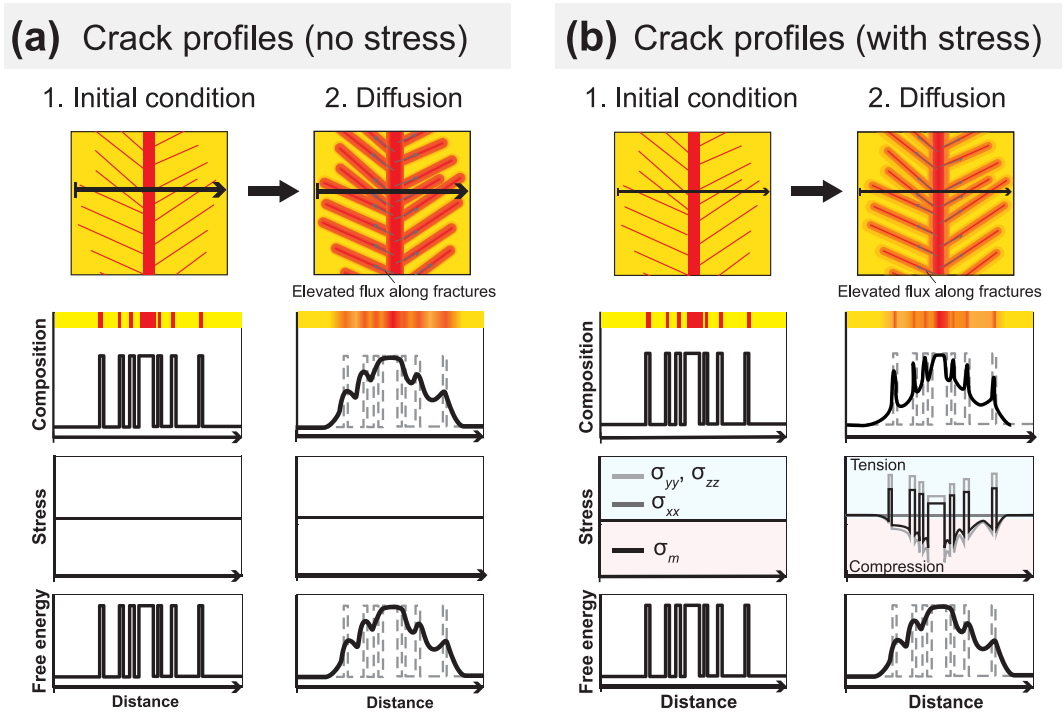

Fig. 7. Conceptual diffusion scenarios for Crack profiles using (a) standard, stress-free diffusion modeling and (b) modeling with compositional stress. A garnet core is crosscut by a large fracture containing a different composition. Smaller microfractures propagate from the main fracture into the garnet core. A 1-D chemical profile transecting the fractures shows the microfractures as local spikes in composition. Also shown are the relative chemical potential (free energy) profiles and stress (σ_{xx}, σ_{yy}, and σ_{zz} are stresses in the x, y, and z directions, and σ_m is the mean stress). In (a), no stress develops as diffusion occurs, and the sharp compositional contacts relax. In (b), stress develops as diffusion occurs, limiting the relaxation of the sharp contacts.

the first eclogite facies garnet rim and is the model initial condition. Diffusional relaxation ensues until a second ICDR reaction replaces part of the garnet rim followed by further diffusional relaxation. Garnets may undergo several sequential ICDR episodes.

As ICDR is typically rapid compared to intracrystalline diffusion (e.g. Putnis, 2002, 2021; Putnis & Austrheim, 2010; Renard *et al.*, 2019), we assume that the ICDR replacement reactions occur essentially instantaneously. We infer the number of episodes of ICDR from the number of distinct garnet rim zones defined by a composition change across zone contacts of at least ±3σ (i.e. spanning a 6σ range). Although ICDR can create compositional heterogeneity (e.g. Pollok *et al.*, 2011; Borg *et al.*, 2014), the compositional variation within each rim zone is normally small relative to the variation between rim zones (e.g. Figs 4f, 5, and 6). Thus, we use uniform compositions for each garnet rim zone in our models.

Diffusion methodology

We use the methodology of Hess & Ague (2023, 2024*a*) to model diffusion. It is based on Larché–Cahn theory (Larché & Cahn, 1982, 1985), which allows for the coupling of stress and chemical diffusion via gradients in the free energy.

Stress in our models is generated by the interdiffusion of different-sized species that strain the crystal lattice. The stresses are analogous to thermal stresses wherein temperature change causes lattice expansion or contraction, and thus, stress. As diffusion and heat conduction follow the same governing equations, diffusion-induced compositional stresses can be quantified using modified spherical or planar thermoelastic equations (Larché & Cahn, 1982). Hess & Ague (2024*a*) develop this approach for quaternary garnet diffusion incorporating linear viscous relaxation following Stephenson (1988) and Erdélyi & Schmitz (2012). See Hess & Ague (2023, 2024*a*) and the Supplementary Information for details.

We assume the garnets are initially at a constant pressure (i.e. stress free) equal to the metamorphic conditions. Stress then develops as diffusion occurs. We neglect any atomic-scale stresses due to initial chemical zonation, which are small if present (e.g. Pollok *et al.*, 2001) and would regardless have no impact on our larger, grain-scale model (Hess & Ague, 2024*a*). Any compositional stress in portions of garnet replaced by ICDR reactions is assumed to be erased. Model initial conditions and the treatment of microfractures and episodic ICDR are as described previously.

We use 680 °C and 2.1 GPa for peak eclogite facies metamorphic conditions (Bhowany *et al.*, 2018) and the diffusion coefficient calibration of Chu & Ague (2015) as modified for spessartine by Chen & Chu (2024). The garnet end-member chemical potentials and activities are calculated using Holland & Powell (2011) and White *et al.* (2014), respectively. The garnet material parameters are 240 GPa for Young's modulus and 0.27 for Poisson's ratio (Erba *et al.*, 2014). We take these values as constant as they vary only slightly with composition, potentially changing the calculated stress magnitude by at most a few percent. We use 10^{24} Pa·s for viscosity (Hess & Ague, 2024*a*).

The interdiffusion coefficients vary spatially and temporally as a function of concentration. The rim composition is assumed to be constant during ICDR events, and otherwise, zero flux boundary conditions are used, specifying no exchange between the garnet and matrix. The widths of the rims are sufficiently large so that the choice of boundary conditions does not affect the

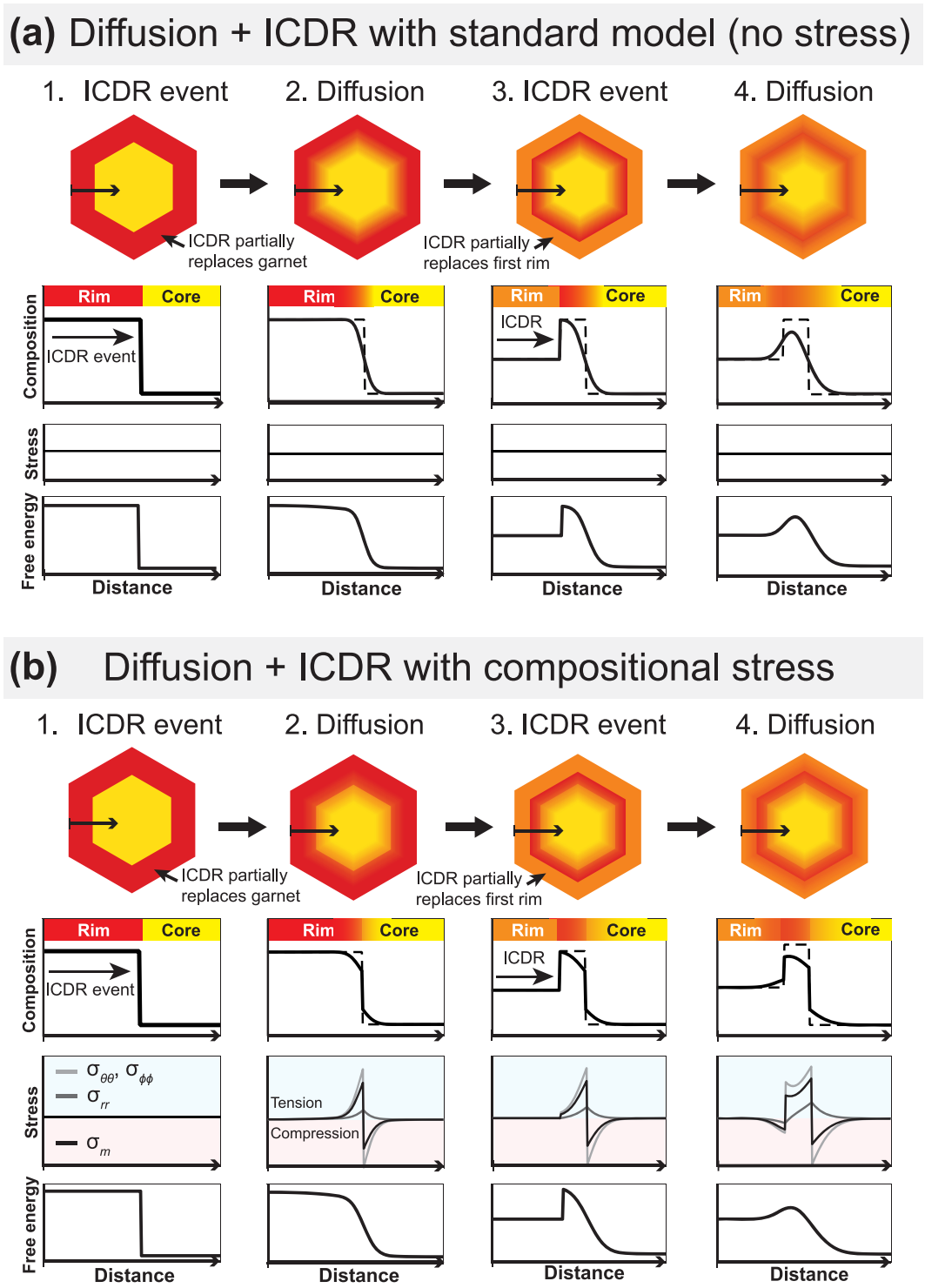

Fig. 8. Conceptual diffusion scenarios for the Rim profiles using (a) standard, stress-free diffusion modeling and (b) modeling with compositional stress. Model stages: (1) ICDR creates a new rim. (2) Diffusion occurs between the core and rim. (3) ICDR creates a second garnet rim. (4) Diffusion continues. For each stage, a 1-D transect shows the evolving composition, internal stress ($\sigma_{\theta\theta}$ and $\sigma_{\phi\phi}$ are tangential stresses and σ_{rr}, radial stress), and relative chemical potential (free energy). In (a), no stress develops and the chemical heterogeneities smooth. In (b), stress develops during diffusion, limiting the relaxation of the initial sharp compositional contacts.

evolution of the core–rim contacts during diffusional relaxation. We apply a convolution correction following the procedure of Ganguly *et al.* (1988) using a convolution factor of 0.48 (Borinski *et al.*, 2012). The best fitting model results are determined using Alm, Prp, and Grs Chi-square statistics. Further details can be found in the Supplementary Information.

Impact of compositional stress on diffusion

Standard diffusion models assume that no stress is generated during diffusion. This is often a reasonable assumption for species with similar sizes as is the case for Fe–Mg interdiffusion in garnet. The extent of diffusional relaxation then allows timescales of metamorphism to be quantified (Figs 7a and 8a;

Chakraborty & Ganguly, 1992; Florence & Spear, 1993; Faryad & Chakraborty, 2005; Carlson, 2006; Ague & Baxter, 2007; Caddick *et al.*, 2010; Ague & Carlson, 2013; Chu *et al.*, 2017).

However, when diffusion occurs between species of different sizes, intracrystalline stresses and strains will develop. The molar volume of Grs is ~9–10% larger than Prp and Alm (Holland & Powell, 2011). Consequently, Ca–Mg–Fe interdiffusion in garnet may produce appreciable stresses and strains that affect diffusion (Hess & Ague, 2024*a*).

Chemical diffusion occurs until the decrease in chemical energy is balanced by the increase in strain energy from stress (Hess *et al.*, 2022; Hess & Ague, 2024*a*, 2024*b*). The increased strain energy makes it energetically unfavorable to fully relax an initially sharp compositional contact, and thus, sharp compositional boundaries diminish but persist indefinitely in perfectly elastic crystals (Hess & Ague, 2024*a*). Nonetheless, the relative chemical potential (free energy) profiles that drive diffusion smooth and relax even when sharp contacts endure (Figs 7b and 8b). If inelastic viscous behavior is incorporated, as in this study, the stresses will eventually dissipate, facilitating the long-term relaxation of sharp contacts.

In the Crack profiles, sharp Grs oscillations diminish in magnitude, but the resulting compositional stress causes them to remain sharp (Fig. 7b). Likewise in the Rim profiles, an initial sharp chemical contact will diminish but remain sharp, developing diffuse limbs on either side that smoothly decay into the two adjacent chemical zones (Fig. 8b). A sharp contact with diffuse limbs is the theoretical profile shape indicating the presence of compositional stress.

We note that interface resistance may produce chemical profiles that appear similar (e.g. Crank, 1979, Fig. 3.7). However, interface resistance stems from limitations on the diffusion rates across an interface. Such limitations are unlikely between coherently bonded garnet zones formed via ICDR. Interface resistance can be distinguished because it will affect all diffusing species regardless of size, whereas compositional stress will be a function of the relative cation sizes, as observed herein.

RESULTS AND DISCUSSION

Diffusion modeling results

The garnet chemical profiles are modeled using either diffusion (Crack profiles; Figs 9 and 10) or diffusion combined with episodic ICDR (Rim profiles; Figs 11–15). A consistent timescale across all chemical profiles is possible only if diffusion-induced compositional stress is considered.

Model results with compositional stress

The Crack profiles capture diffusion between the granulite garnet core and eclogite facies fractures and microfractures (Figs 5a, c and 7). The 43F and 46A Crack profiles give best fitting timescales of 300 and 320 kyr, respectively, when modeled at peak pressure eclogite facies conditions (Figs 9a and 10a). The profile initial conditions (dashed gray lines) take the spikes in X_{Grs} adjacent to the main fracture to be locations of intersecting microfractures (see Fig. 7). However, these initial conditions lead to a large discrepancy in the mass balance of Prp and Alm between the model compared to the observed profile (solid dark gray lines in Figs 9a, b and 10a, b). The discrepancy indicates that the microfractures acted as fast vacancy-mediated or fluid-mediated diffusion pathways. We find that the mass balance is achieved for both the 46A and 43F crack profiles with t_b values (the effective duration of elevated flux) of 50 kyr (see Eq. (2)). The consistent t_b values indicate that the microfractures in both garnets facilitated similar rates of elevated material flux into the garnet cores.

The model results predict that 100 s of MPa of differential stress develop at the micrometer scale due to diffusion (Figs 9a and 10a). These stresses prevented the relaxation of sharp X_{Grs} oscillations, most notably those in the 43F Crack profile (Fig. 9c), and may also have contributed to the formation of the observed microfractures (e.g. Scheidl *et al.*, 2014).

The Rim profiles yield consistent timescales of 280 kyr (46A Rim and 8A Rim 2; Figs 14c and 15a), 290 kyr (8A Rim 1; Fig. 14a), 300 kyr (43F Rim; Fig. 13a), and 310 kyr (16A Rim 1 and 2; Figs 11a and 12a). Both diffusion and episodic ICDR reactions are required to reproduce the observed profiles, with all garnet rims recording at least two episodes of ICDR.

The 16A Rim profiles 1 and 2 show most clearly the replacement of older garnet rims (Figs 11a and 12a). Profile 1 displays two garnet rims with the second partially replacing the first (Fig. 11a). Diffusional relaxation between the rim zones provides both the overall timescale and timing of the second ICDR reaction relative to the first. Within the overall 310-kyr timescale, the second ICDR reaction occurred 180 kyr after the first. Profile 2 has an even greater asymmetry and only preserves the second rim. Although only one garnet rim is evident, we assume that because both profiles were collected from the same garnet, profile 2 likewise had an earlier rim of the same composition seen in profile 1 that was fully replaced at 180 kyr (Figs 4e, f and 11a). With this assumption, we reproduce the asymmetric profile at 310 kyr (Fig. 12a).

The 43F Rim profile is likewise highly asymmetric, indicating two episodes of ICDR. The profile gives a total timescale of 300 kyr with a second rim forming 130 kyr after the first (Fig. 13a). The 8A Rim profiles 1 and 2 yield timescales of 290 and 280 kyr, respectively, and reveal four unique rim compositions, implying four fluid pulses (Fig. 14a and c). The second pulse occurred at 160 kyr (profile 1) or 150 kyr (profile 2), and the third and fourth pulses at 210 and 230 kyr for both profiles. The slight variation in best fitting timescales is attributed to analytical uncertainty. Finally, the 46A Rim profile gives a total timescale of 280 kyr (Fig. 15a). It also reveals multiple garnet rim generations with timings of 150 and 210 kyr after the first rim formed.

Our modeling predicts that large compositional stresses develop during diffusion, reaching up to 400 MPa. The 43F Rim profile has the largest stress as it has the greatest initial difference in X_{Grs} across the core–rim contact (Fig. 13a). Stress limits the relaxation of the sharp contact, consistent with theoretical predictions (Figs 8 and 13c). The least compositional stress develops in the 46A Rim profile, which exhibits dominantly Mg–Fe interdiffusion. The large difference in X_{Alm} and X_{Prp} nonetheless leads to 100 MPa differential stress (Fig. 15a). Thus, Fe–Mg interdiffusion can still generate appreciable stresses, but in our case, they are not large enough to meaningfully alter diffusion chronometry results compared to a standard, stress-free diffusion model (Fig. 15b).

The modeled stress magnitudes are consistent with the extensive microfracture networks propagating from the core–rim boundaries in 43F garnet chemical maps (Fig. 2a, c, g). The spikes in X_{Grs} on the core side of the core–rim contact in the 43F Rim profile are inferred to be microfractures that facilitated fast diffusion into the core as in Crack profiles. Without this assumption, the large hump in X_{Alm} in the profile cannot be reproduced (Figs 5b and 13). Like the Crack profiles (Figs 9 and 10), we obtain a t_b value of 50 kyr, suggesting that the microfractures in this profile facilitate a similarly elevated and rapid diffusion rate.

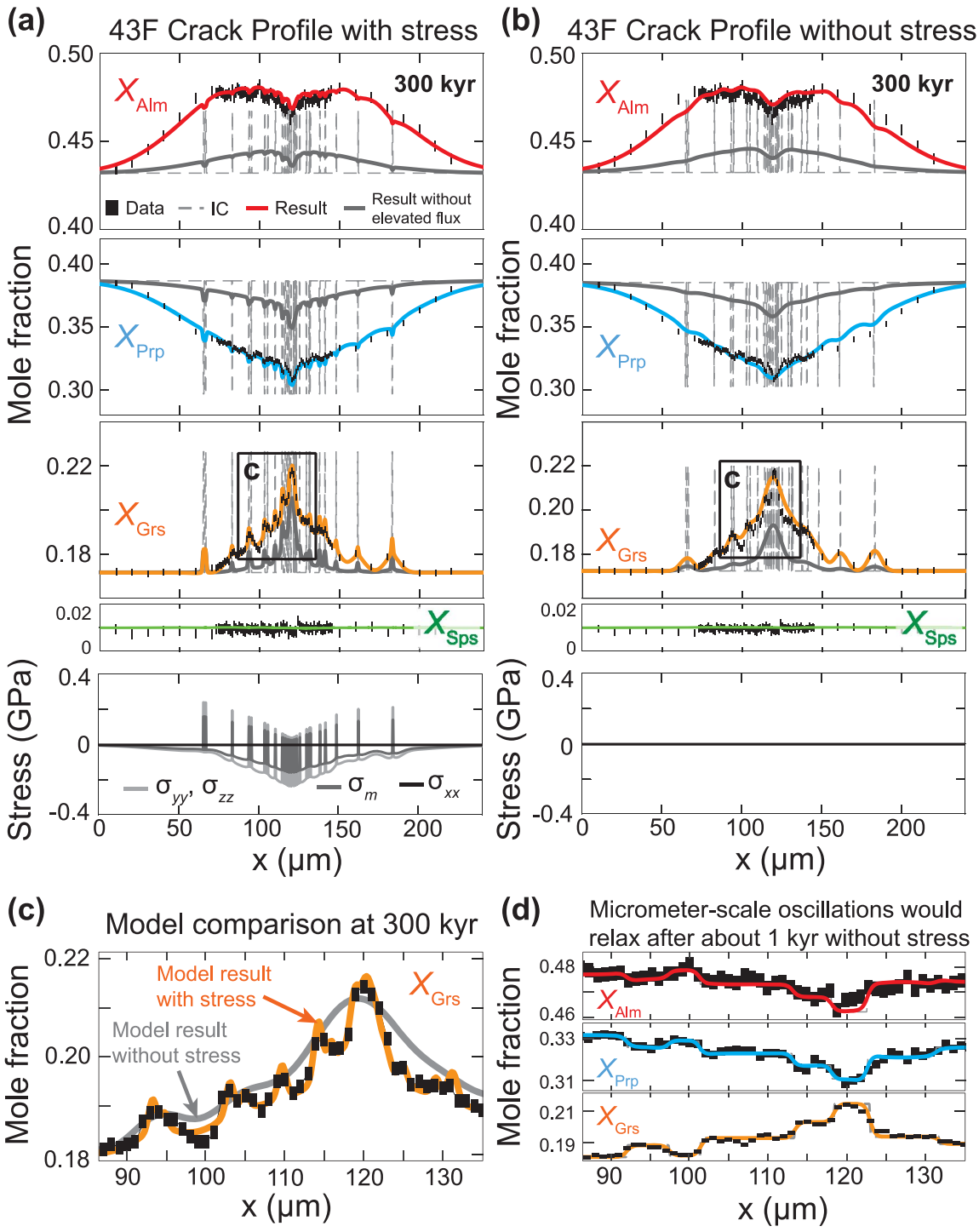

Fig. 9. Model results for the 43F Crack profile (a) with compositional stress and (b) without compositional stress. Gray dashed lines depict the initial conditions (IC), which are a series of step functions representing intersected microfracture networks (Fig. 7). The solid dark gray lines denote the model results without elevated flux (see text). (c) Detailed comparison of the Grs profiles at 300 kyr showing the relaxation of the micrometer-scale oscillations without compositional stress. (d) Without compositional stress, the micrometer-scale oscillations imply ~1 kyr of diffusion in clear contradiction to the extent of Alm and Prp diffusion in (a) and (b).

In summary, the Crack and Rim profiles provide a consistent timescale of 280–320 kyr (Fig. 16a). We emphasize that the geologic interpretation of this timescale is complex, as it may include pulsed eclogite facies activity as well as retrogression (see below). Regardless, it is clear that the diverse profile morphologies can be explained and reproduced by combining diffusion, compositional stress, microfractures, and episodic ICDR (Figs 9–15).

Standard model results without compositional stress

Modeling without compositional stress yields significantly different timescale estimates for different samples and is unable to reproduce the full-profile morphologies.

The timescales for the Crack profiles remain 300 and 320 kyr based on the length scale of Alm and Prp diffusion beyond the microfracture zone (~30 μm; Figs 9b and 10b). However,

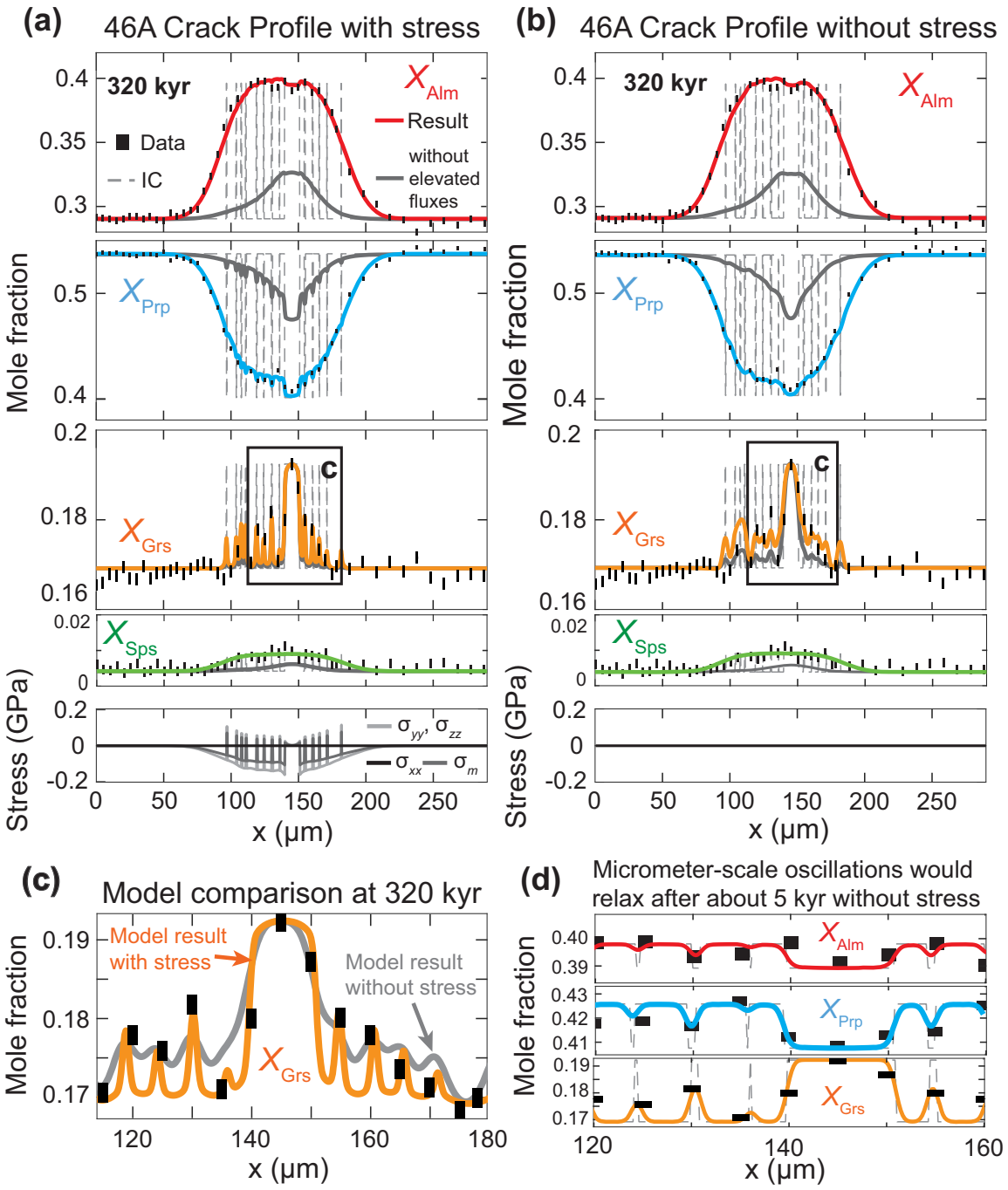

Fig. 10. Model results for the 46A Crack profile (a) with compositional stress and (b) without compositional stress. (c) Detailed comparison of model results. (d) Without compositional stress, the micrometer-scale oscillations imply ~5 kyr of diffusion in clear contradiction to the extent of Alm and Prp diffusion in (a) and (b). See Fig. 9 for additional information.

micrometer-scale Grs oscillations cannot be reproduced at the longer timescales as they relax in standard diffusion models (Figs 9c and 10c). The maximum timescale for which these micrometer-scale oscillations can be preserved without stress is ~1 kyr in the 43F Crack profile (Fig. 9d) and 5 kyr in the 46A Crack profile (Fig. 10d).

Similarly, Alm and Prp indicate far longer timescales than implied by sharp Grs features in the 8A, 16A, and 43F Rim profiles. The 300-kyr timescale for the 43F Rim profile reproduces the diffuse Prp and Alm limbs using standard diffusion methods (Fig. 13b), but they fail to reproduce the sharp core–rim contact (Fig. 13c). If the sharpness of the contact alone is used to estimate a timescale, the standard diffusion method results are an order of magnitude shorter (26 kyr; Fig. 13d).

Likewise, 16A Rim profile 1 indicates a total timescale of 310 kyr based on Alm and Prp diffusion, but at this timescale, standard diffusion methods predict much greater relaxation of the large Grs step at the core–rim contact (Fig. 11c). The Grs sharpness suggests a 20-kyr timescale using standard methods (Fig. 11d). In contrast, 16A Rim profile 2 collected from the same garnet has a small Grs step at the core–rim contact and gives a consistent

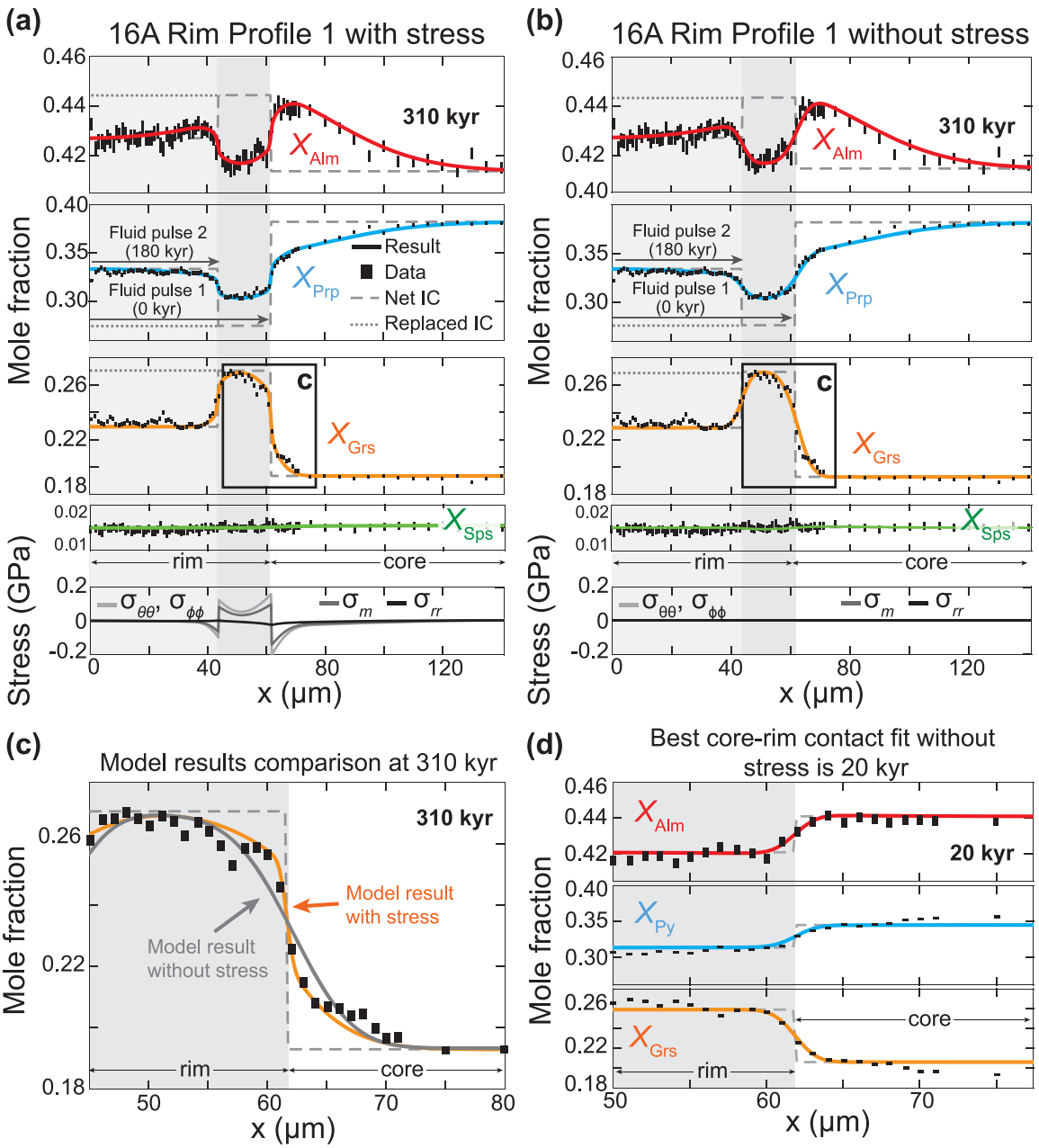

Fig. 11. Model results for 16A Rim profile 1 (a) with compositional stress and (b) without compositional stress at 310 kyr. Here and below, the profiles are formed by multiple fluid pulses that replace older rim compositions. The dashed lines indicate the cumulative initial condition (Net IC) from all fluid pulses whereas the dotted lines indicate rim compositions that have been replaced (Replaced IC). (c) Detailed comparison of model results for the core–rim contact at 310 kyr. (d) Using standard diffusion modeling (no stress), the sharp core–rim contact implies a much shorter timescale of 20 kyr.

timescale of 310 kyr with or without stress based solely on Alm–Prp interdiffusion (Fig. 12).

For 8A Rim profile 1, Alm–Prp interdiffusion yields a 290-kyr timescale (Fig. 14a) but the sharp Grs core–rim contact implies only 29 kyr (Fig. 14b). On the other hand, 8A Rim profile 2 has little Grs variation at the contact and gives consistent timescales of 280 kyr with or without stress (Fig. 14c and d). Finally, the 46A Rim profile timescale result is the same with or without compositional stress as there is negligible Grs variation at the core–rim contact (280 kyr; Fig. 15).

The characteristics of the Crack and Rim profiles (Figs 9–15) substantiate the theoretical predictions of compositional stress: interdiffusion of different-sized species will generate compositional stress that limits the relaxation of sharp contacts (e.g. 43F Rim profile; Fig. 13a) whereas similar-sized species will not generate appreciable stresses, leading to standard diffusion behavior (e.g. 46A Rim profile; Fig. 15). Neglecting compositional stress leads to inconsistent timescale results with the shortest timescales being an order of magnitude or more too short (Fig. 16a).

The impact of compositional stress is independent of diffusion coefficient calibration or uncertainties on eclogite facies pressure and temperature conditions. Although we use the calibration of Chu & Ague (2015), the disparate timescales would remain with any other calibration (e.g. Chakraborty & Ganguly, 1992; Carlson, 2006; Vielzeuf *et al.*, 2007). The absolute values inferred for the timescales may shift somewhat, but the order of magnitude difference between the timescales suggested by the sharp contacts and

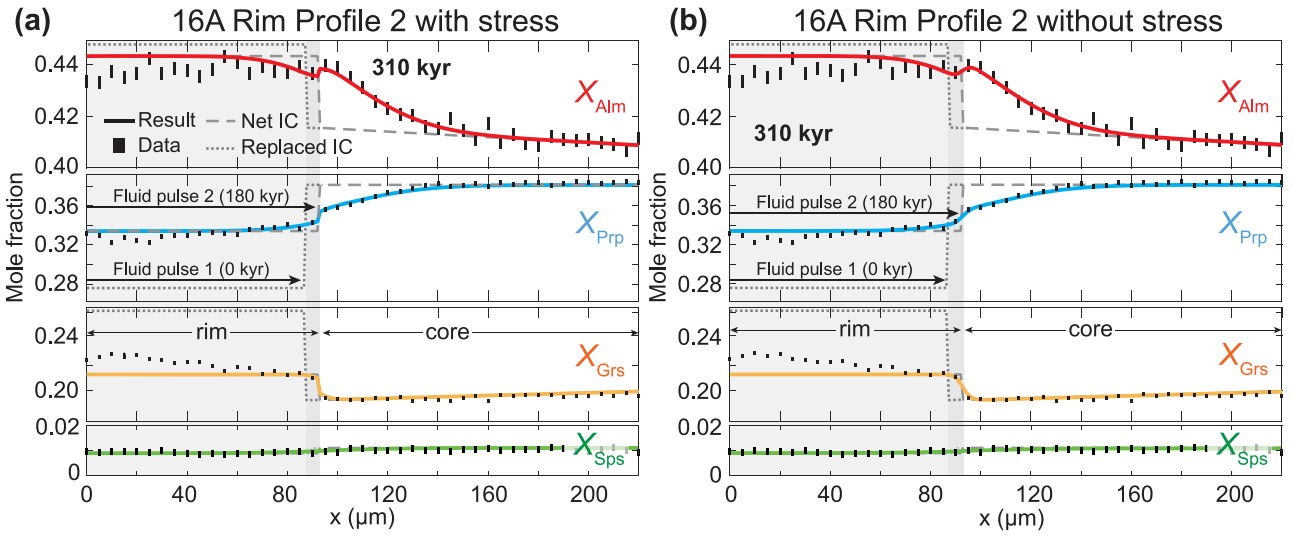

Fig. 12. Model results for 16A Rim profile 2 (a) with compositional stress and (b) without compositional stress. Both models give the same timescale based on the Alm and Prp profiles. 16A Rim profile 2 was collected along the same rim as profile 1, which records two rim generations (Fig. 4e). Thus, we infer the first garnet rim (fluid pulse 1) was originally present but has been completely erased by the later fluid pulse 2. The composition of the first rim is inferred from 16A Rim profile 1 (Fig. 11).

diffuse limbs would remain (Fig. 16a). Additionally, the sharp contacts cannot be explained by composition dependence in diffusion coefficients. This could contribute to asymmetry but is unable to preserve a sharp contact that requires something, such as strain energy, to offset the decrease in chemical energy from diffusion between different compositional domains.

Uncertainties

Timescale uncertainties were estimated using a Monte Carlo forward model incorporating uncertainties on temperature, pressure, and diffusion coefficients (Chu & Ague, 2015). We evaluated the 46A Rim profile because it is simple and symmetric (Fig. 15). Bhowany *et al.* (2018) give 670–690 °C and 2.1–2.2 GPa ranges for peak pressure eclogite facies conditions. Taking this as 680 ± 10 °C and 2.15 ± 0.5 GPa (1σ) yields a $^{+110}_{-85}$ kyr timescale uncertainty (1σ), which pertains to the absolute accuracy of the results. The precision of one sample timescale result relative to another is significantly better (smaller ± range; Chu & Ague, 2015).

Summary of results and comparison with previous garnet diffusion chronometry

The consistent 280- to 320-kyr timescale across all samples indicates that the peak pressure eclogite facies conditions (680 °C and 2.1 GPa) lasted for a maximum of c. 300 kyr. Other commonly used garnet diffusion calibrations would provide similar or somewhat shorter durations (e.g. Chakraborty & Ganguly, 1992; Carlson, 2006). Over the likely range of eclogite facies *P–T* conditions for Holsnøy (Bhowany *et al.*, 2018), the diffusion coefficients do not undergo large changes and are similar to those used herein for peak pressure conditions. Thus, ~300 kyr is also the approximate timescale of eclogite facies metamorphism.

We emphasize that this ~300-kyr timescale must be interpreted very carefully. For example, it could represent a single event, or it could represent an integrated series of relatively short eclogite facies episodes separated by intervening lower grade periods during which less diffusion occurred (e.g. van Haren *et al.*, 1996; Camacho *et al.*, 2005; Ague & Baxter, 2007). In the latter case, the individual episodes could integrate to ~300 kyr of eclogite facies diffusion, but the total duration of metamorphism would be longer. As any diffusion that took place during the intervening lower grade periods would contribute to the total amount of relaxation measured in the garnets, ~300 kyr represents a maximum cumulative duration of eclogite facies conditions. Importantly, regardless of whether the eclogite facies metamorphism was continuous in time or episodic, appreciable additional diffusion may have occurred during retrogression. Therefore, the true eclogite facies timescale is almost certainly less than ~300 kyr because the diffusion profiles include both eclogite facies and any retrograde diffusion.

To summarize, ~300 kyr is the 'maximum' time the rocks could have been in the eclogite facies. This is true whether the eclogite facies metamorphism was a single continuous event, or a series of shorter, more widely spaced episodes that integrate to ~300 kyr at eclogite facies conditions. We explore these issues further in the following sections.

Our results are consistent with and can explain the disparate findings of past work. Previous studies that interpreted a longer 10^5- to 10^6-yr duration of eclogite facies metamorphic conditions were based on garnet crystals with dominantly Fe–Mg interdiffusion (Erambert & Austrheim, 1993; Perchuk, 2002). For example, Perchuk (2002) estimated cooling from peak eclogite facies to amphibolite facies conditions in 0.8 Myr. In their model, ~95% of the diffusion occurred at high temperatures (>650 °C) in ~500 kyr, consistent with our results. Erambert & Austrheim (1993) arrived at longer timescales of 1–4 Myr at 700 °C by estimating the characteristic length scale (or penetration depth) of diffusion: $x \sim \sqrt{Dt}$ where x is the length scale (m), D is the diffusion coefficient (m^2 s^{-1}), and t is time (s). However, their length scale (30–50 μm) actually represents about four times the characteristic length scale ($x \sim 4\sqrt{Dt}$) (e.g. Fig. 6.14 in Philpotts & Ague, 2022). Using the corrected length scale ($4\sqrt{Dt}$) together with their calculated interdiffusion coefficient yields ~0.1–0.2 Myr, consistent with Perchuk (2002) and this study (Fig. 16a).

Raimbourg *et al.* (2007*a*) estimate a long metamorphic duration of 8–12 Myr based on Fe–Mg interdiffusion in garnet from Holsnøy. The length scale of the crack profile they model is ~135 μm

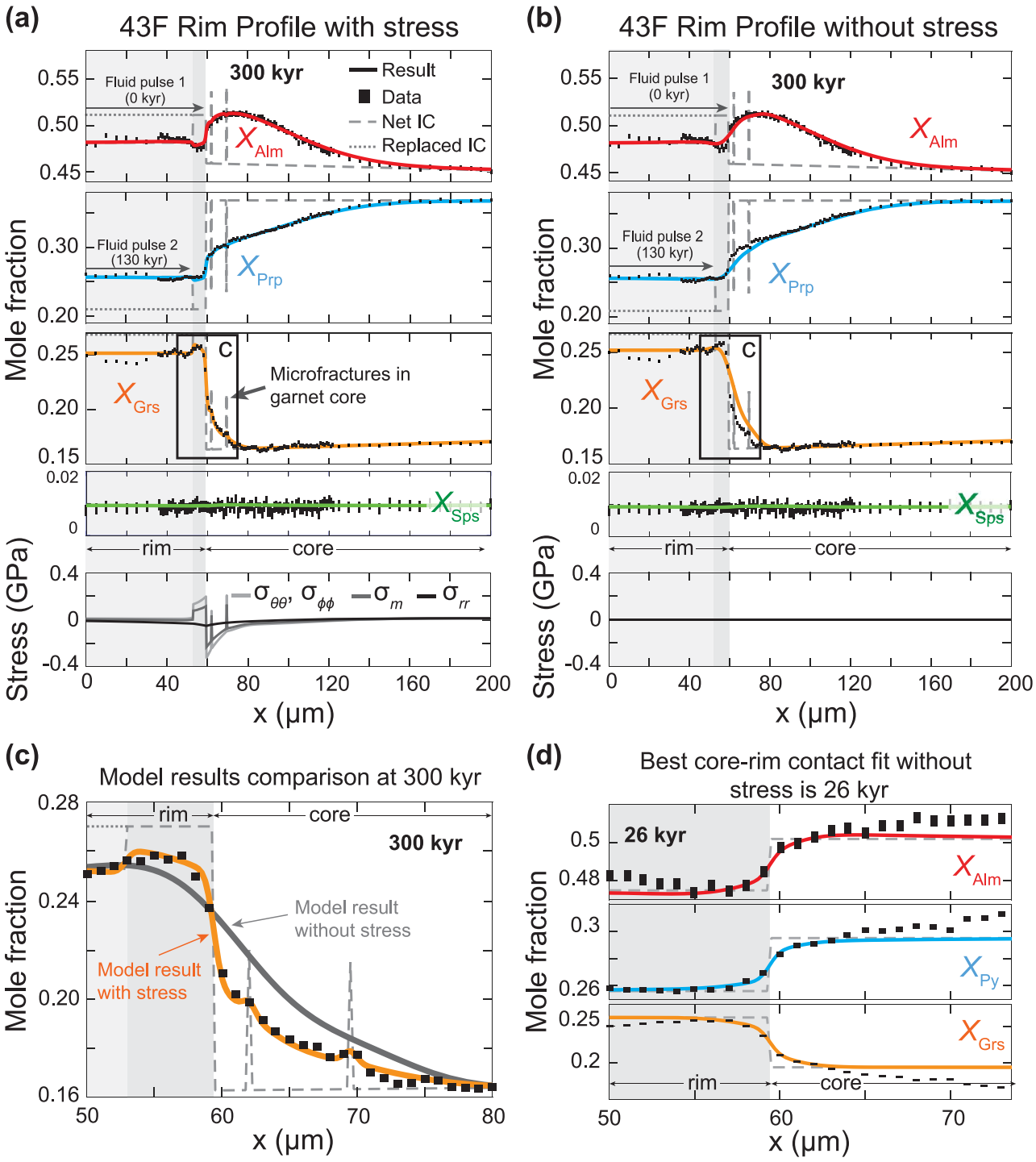

Fig. 13. Model results for the 43F Rim profile (a) with compositional stress and (b) without compositional stress at 300 kyr. (c) Detailed comparison of model results for the core–rim contact at 300 kyr. (d) Using standard diffusion modeling (no stress), the sharp core–rim contact implies a much shorter peak timescale of 26 kyr.

using the relationship $x \sim 4\sqrt{Dt}$ (their Fig. 15). However, this is three to four times wider than profiles measured by Erambert & Austrheim (1993), Perchuk (2002), and this study, all of which find a consistent 30–50 μm length scale (e.g. Figs 10 and 15). Moreover, Raimbourg *et al.* (2007*a*) show that the Fe–Mg diffusion bands in some of their other garnets are also ~50 μm wide (e.g. their Figs 4 and 10). We speculate that the 135 μm length scale may be artificially long owing to factors including ICDR, microfracturing adjacent to the main crack, and/or a tilted or irregular chemical interface. The shorter ~50 μm length scales give 200–250 kyr for eclogite facies conditions using their characteristic temperature (700 °C) and an Fe–Mg interdiffusion coefficient of 2×10^{-23} m^2 s^{-1} (Chu & Ague, 2015). Thus, our results and the Fe–Mg interdiffusion documented in previous studies indicate 100- to 500-kyr timescales.

In addition, Raimbourg *et al.* (2007*a*) observed extremely sharp X_{Grs} rim contacts that suggested eclogite facies metamorphism lasted at most 0.14–32 kyr, which is similar to the

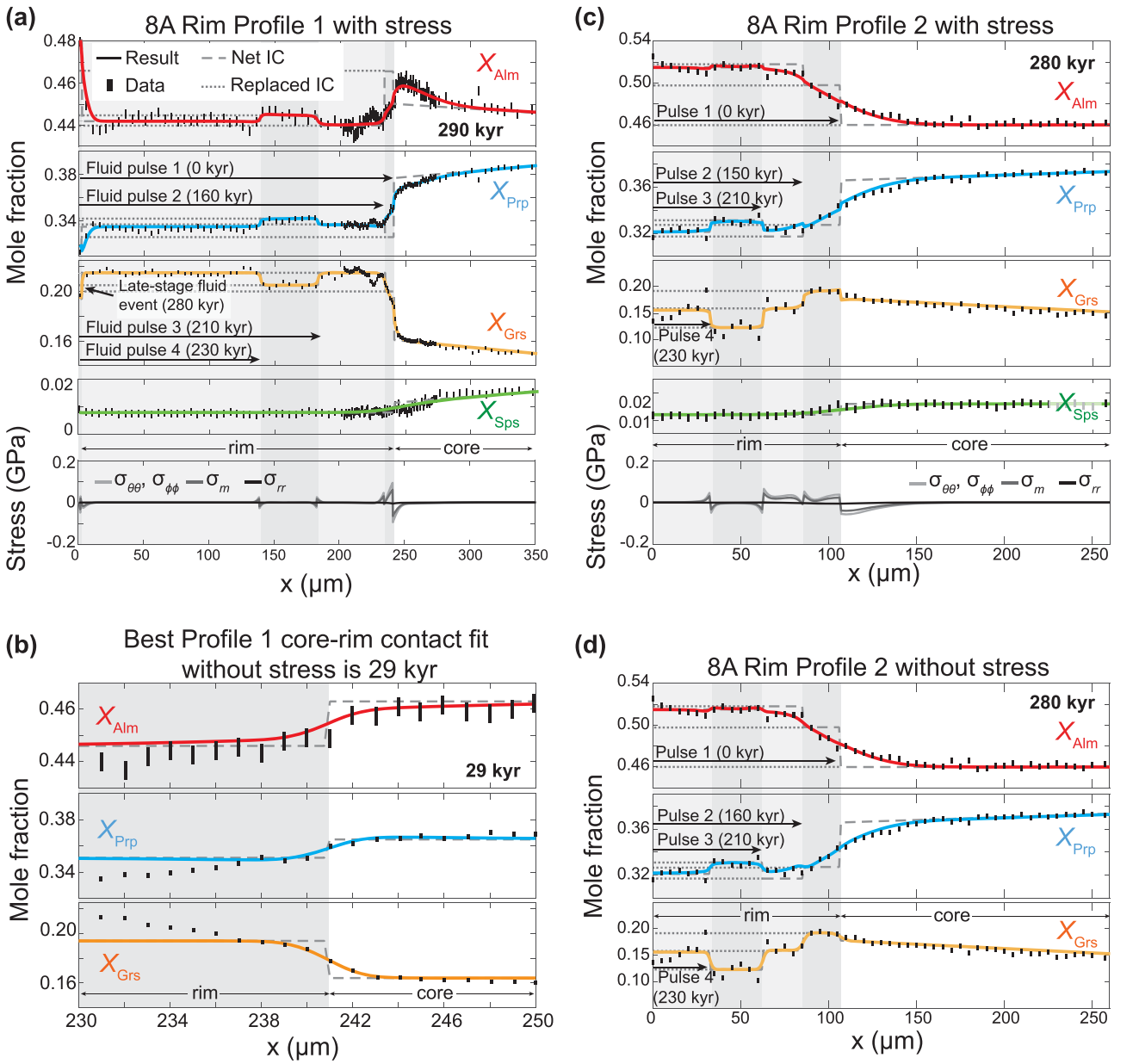

Fig. 14. Model results for 8A Rim profiles 1 and 2. (a) Profile 1 gives a 290-kyr timescale with compositional stress that reproduces the broad Alm and Prp and sharp Grs features whereas in (b) the sharpness of the core–rim contact gives a 29-kyr timescale without stress that does not reproduce the broad Alm and Prp features. Profile 2 gives a 280-kyr timescale based on Alm and Prp (c) with stress and (d) without stress.

1- to 29-kyr timescales we obtained from sharp contacts and micrometer-scale oscillations when using standard, stress-free diffusion modeling (Fig. 16a). Raimbourg *et al.* (2007*a*) interpreted the timescales estimated from diffuse Fe–Mg curves and sharp Ca contacts to represent distinct metamorphic events. Nonetheless, they note that the lack of Ca diffusion in the assumed earlier event cannot be explained thermodynamically, and they instead argue for a kinetic limitation on Ca availability (Raimbourg *et al.*, 2007*a*).

Our study provides a simple alternative explanation: the diffuse Fe–Mg curves and sharp Ca contacts represent the same, longer duration metamorphic event. Accounting for compositional stress allows sharp X_{Grs} features to be reproduced at the longer timescales indicated by the diffuse X_{Alm} and X_{Prp} features (Fig. 16a).

Multiple fluid pulses

The dry, metastable granulite of Holsnøy was an ideal setting for preserving a record of fluid flow, as fluid reacted strongly during infiltration. Fluids are thought to have been sourced from an underlying metasedimentary unit (Jamtveit *et al.*, 1990, 2021; Mattey *et al.*, 1994) with possible local contribution from granulite facies scapolite (Putnis *et al.*, 2017).

All garnets have at least two rim generations formed by distinct episodes of eclogite facies fluid infiltration and ICDR (Fig. 16b). The degree of diffusional relaxation of different generations of garnet rims allows us to estimate the relative timings of rim formation. We present non-dimensionalized results for the relative timings of the fluid pulses to allow flexibility in applying different model scenarios. The timing of each fluid pulse (t) is divided by the total time estimate for eclogite facies conditions

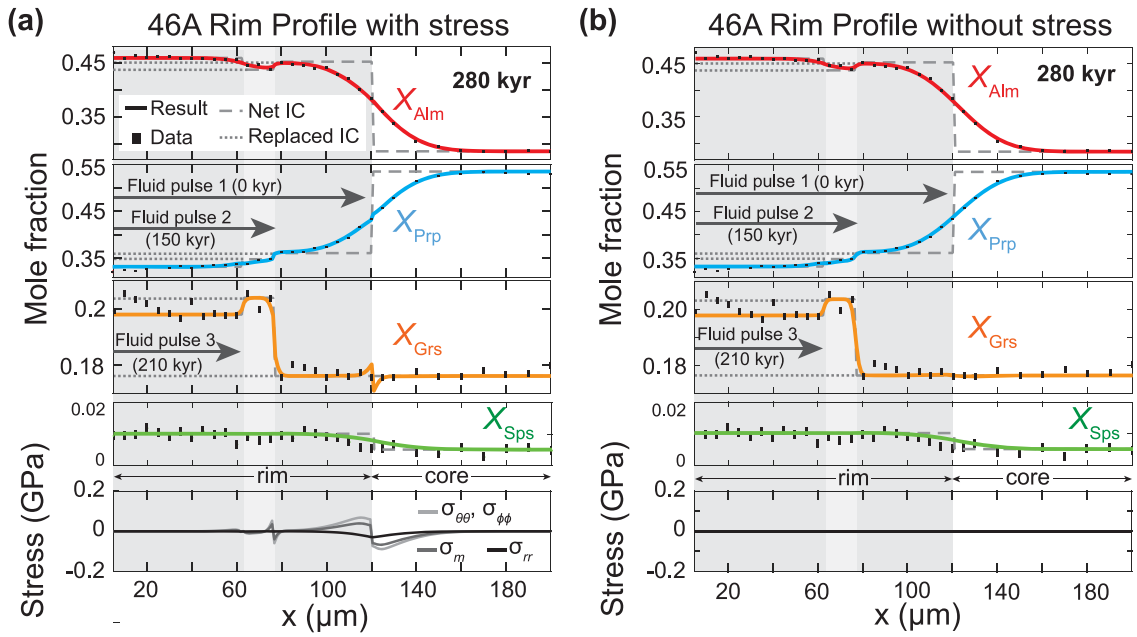

Fig. 15. Model results for the 46A Rim profile (a) with and (b) without compositional stress. Both models give similar timescales based on the Alm and Prp profiles.

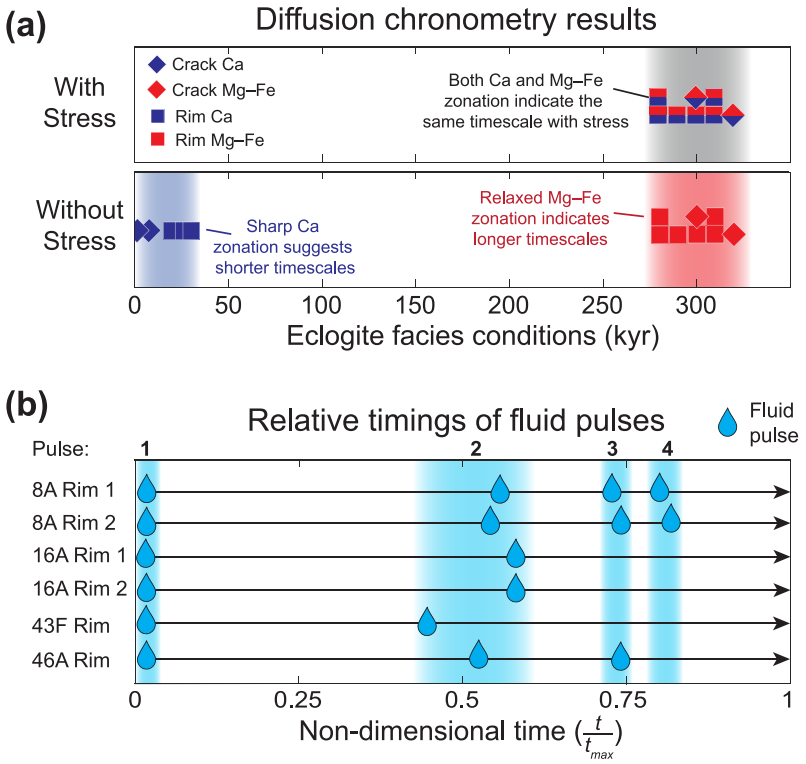

Fig. 16. Diffusion chronometry results. (a) Maximum eclogite facies metamorphism timescales from model results with and without compositional stress. Without compositional stress, samples yield both short 1- to 29-kyr timescales based on sharp Grs features and longer 280- to 320-kyr timescales based on smooth Prp and Alm profile curves. In contrast, when compositional stress is considered, the Alm–Prp–Grs zoning in all samples gives a consistent timescale of 280–320 kyr, thus reconciling the strongly discrepant timescale results obtained from standard (without stress) diffusion modeling. (b) Relative timings of fluid pulses for each garnet Rim profile given in non-dimensional time ($\frac{t}{t_{max}}$) where t is time and t_{max} is the total timescale.

(t_{max}; Fig. 16b). For example, in 16A Rim profile 1, the second rim forms 180 kyr after the first (Fig. 11a). Relative to the total 310-kyr timescale (t_{max} at peak pressure conditions), the rim formed 58% of the way through the metamorphism in terms of total diffusion (a non-dimensional value of 0.58). If transient heating episodes occurred over a longer metamorphic timescale, then t_{max} may be, for example, 2.0 Myr, which means that a non-dimensional time of 0.58 corresponds to ~1.2 Myr.

We assume the first fluid pulse occurred at the same time across samples given their consistent results for the maximum

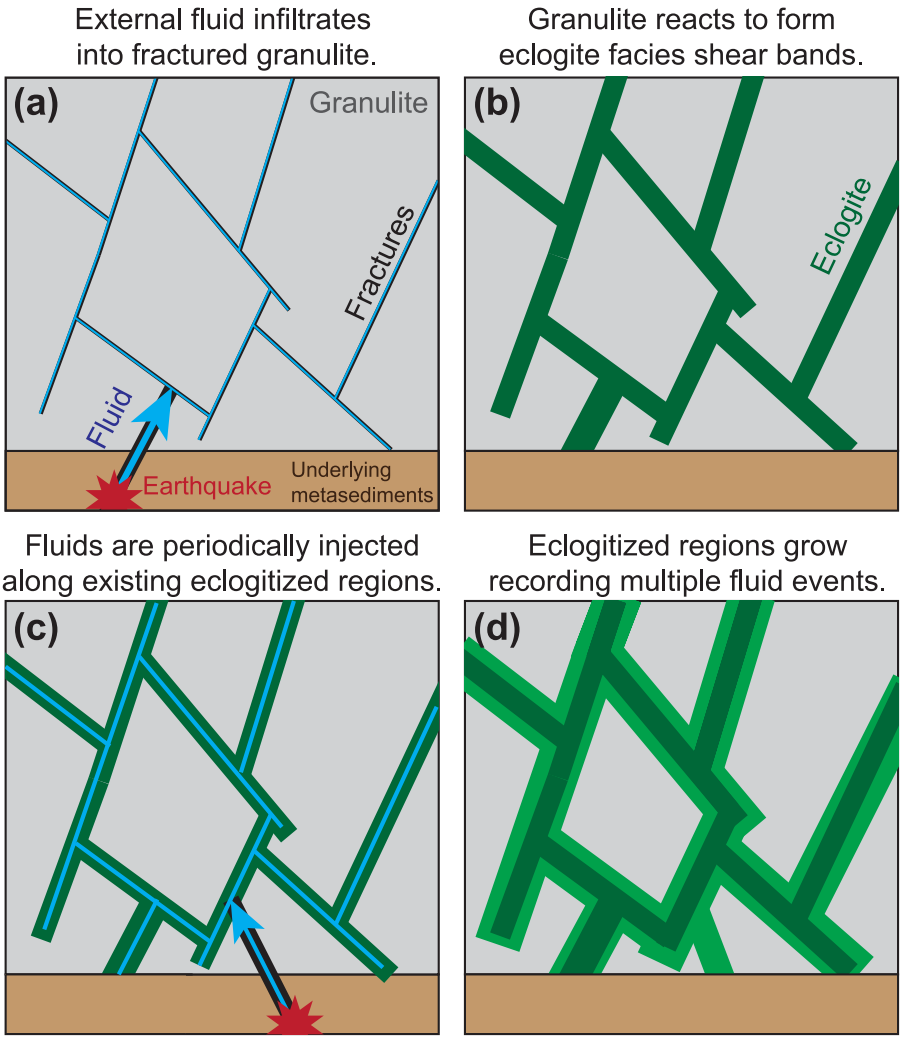

Fig. 17. Holsnøy eclogitization occurring via pulsed, channelized fluid flow. (a) External fluid infiltrates into fractures, shear zones, and other conduits. (b) The infiltrating fluid reacts to form eclogite facies shear bands around unreacted granulite blocks. (c) Subsequent seismic events inject fluids that are preferentially channeled through existing eclogitized channels. (d) The eclogitized regions grow, recording multiple fluid events.

duration of eclogite facies metamorphism (Figs 16a and 17a). We find that all garnets have a second rim that formed approximately halfway through the metamorphic event in terms of total diffusion (Fig. 16b). The agreement across all samples suggests that once the main shear zones and fractures formed, any additional fluid flux in the region was dominantly channeled through them (Fig. 17b–d). Garnets from samples 8A and 46A record a third pulse at 75% of the total diffusion timescale, and the 8A garnets record a fourth pulse at 80%. These additional fluid pulses imply that smaller, more localized fluid infiltration episodes occurred after the two earlier, most regionally extensive ones (Fig. 16b).

The compositional similarity between these garnet rim zones suggests they were all formed at eclogite facies conditions. As a consequence, the eclogite facies metamorphic history accounts for at least 80% of the total diffusion recorded by garnet. Retrogression, therefore, would account for up to 20% of the remaining diffusion. This means that the maximum duration of eclogite facies metamorphism was as much as 20% shorter than the c. 300-kyr value we have determined. Consistently, 8A garnets record high-Fe alteration on their outermost rims that substantially deviates from the other garnet rim zone compositions (Fig. 4c). Diffusion modeling suggests these features formed very late (Fig. 14a). The late formation combined with the composition difference suggests that the fluid pulse and alteration indeed occurred during post-eclogite facies retrogression.

The inferred pulsed fluid infiltration is consistent with the lack of continuous prograde features in the eclogite facies assemblages. The rocks instead capture ‘snapshots’ of pressure and temperature evolution (Bhowany *et al.*, 2018; Putnis *et al.*, 2021; Zertani *et al.*, 2022). The first and second pulses may be tied to stages 1–2 (675–685 °C and 1.5–1.6 GPa) and stage 3 (670–690 °C and 2.1–2.2 GPa), respectively, of eclogite facies metamorphism and fluid infiltration inferred by Bhowany *et al.* (2018). This would imply that the first pulse occurred at the onset of eclogite facies conditions and the second pulse at peak pressure conditions, but further testing is necessary.

Subduction zone seismicity may have exerted important controls on pulsed fluid infiltration (Austrheim, 2013; Jamtveit *et al.*, 2018*a*). Pseudotachylytes associated with eclogite facies shear zones suggest that seismic fracturing on Holsnøy provided the conduits for fluids. The fluids likely further catalyzed fracturing and seismicity via volume reduction and reactive weakening (e.g. Austrheim *et al.*, 1997; Jamtveit *et al.*, 2000, 2019; Bjørnerud *et al.*, 2002; Austrheim, 2013; Bhowany *et al.*, 2018). In addition to seismicity on Holsnøy, we posit that the pulses themselves were tied to cycles of seismic fluid release deeper in the subduction zone

given the episodic nature of the fluid flux (Fig. 17; e.g. Sibson, 1990; Ague *et al.*, 1998; Miller *et al.*, 2003; Camacho *et al.*, 2005; Miller, 2013; Chaves & Schwartz, 2016; Jamtveit *et al.*, 2019; Bras *et al.*, 2021; Dal Zilio & Gerya, 2022).

In summary, multiple generations of eclogite facies garnet rims separated by considerable intervals of diffusional relaxation indicate that fluid infiltration occurred as a series of pulses rather than continuous fluid flow (Fig. 16b). While this is broadly consistent with previous studies (e.g. Erambert & Austrheim, 1993; Bjørnerud *et al.*, 2002; Camacho *et al.*, 2005; Kaatz *et al.*, 2021; Putnis *et al.*, 2021), our new methods resolve discrete fluid pulses and their relative timings (Fig. 16b).

We note that although we have assumed the pulses to be fluid, they could likewise be pulses of melt because melt can also facilitate ICDR (e.g. Gardner *et al.*, 2025). Thus, our use of the term 'fluid' herein is very general and does not necessarily preclude a role for melt (e.g. Jamtveit *et al.*, 1990, 2021).

Tectonic implications

The maximum time that Holsnøy could have been at eclogite facies conditions (670–700 °C and 1.5–2.2 GPa; Bhowany *et al.*, 2018) was c. 300 kyr with retrogression likely reducing this value by up to 20% (Fig. 16). This result is internally consistent among samples, providing a robust constraint for understanding the tectonometamorphic evolution of the region.

The relatively short, c. 300-kyr timescale is difficult to reconcile with standard thermal models of slow regional burial and exhumation. To illustrate, let us assume that eclogite facies metamorphism was continuous for a specified time interval, after which simple linear cooling occurred. More complex cooling paths are undoubtedly possible, but our concern is to establish general tectonic viability. Following Bhowany *et al.* (2018), the cooling from eclogite facies conditions begins at 690 °C and 1.65 GPa in the model.

We can estimate the slowest possible linear cooling rate for this type of model by assuming that the eclogite facies metamorphism was instantaneous, and the observed diffusion all took place during retrograde cooling. This is grossly inconsistent with the presence of multiple generations of eclogite facies garnet rims and fractures, as well as their timing (Fig. 16b), but it nonetheless quantifies the minimum end-member. Even in this extreme scenario, we find that the cooling rate must be 200 °C/Myr to match observations (Fig. S2). Otherwise, the diffusion profiles would be more relaxed than observed. Perchuk (2002) calculated a comparable rate of 160 °C/Myr using the same assumptions. We emphasize that the 200 °C/Myr minimum is extremely fast. Moreover, it is unrealistic as it assumes zero duration for the eclogite facies metamorphism.

Alternatively, we can incorporate the important constraint that eclogite facies fluid pulses were still occurring ~80% of the way through the integrated eclogite facies history (Fig. 16b), corresponding to c. 240 kyr assuming continuous eclogite facies conditions. If we stipulate that cooling commenced immediately afterward, then the calculated cooling rate is at least 2000 °C/Myr (Fig. S2). If eclogite facies temperatures lasted beyond the formation of the final eclogite facies garnet rims, the cooling rate would have to have been even faster.

Obviously, cooling rates of this magnitude are inconsistent with typical regional burial and exhumation. Moreover, the c. 300-kyr timescale is also problematic for baric evolution. Bhowany *et al.* (2018) proposed that eclogite facies metamorphism began at ~1.5–1.6 GPa followed by compression to peak conditions of 2.1–2.2 GPa before decompression back to 1.6–1.7 GPa, all the while at 670–700 °C. Altered garnet rims coexisting with plagioclase indicate that alteration and diffusion began prior to peak pressure eclogite facies conditions (Bras *et al.*, 2021; Putnis *et al.*, 2021; Zertani *et al.*, 2022), and thus, our timescale results span the apparent compression and decompression.

Consequently, eclogite facies compression and decompression would have required at least 12 cm/yr combined burial and exhumation rates, assuming a 300-kyr timescale and lithostatic pressure variations. These rates are at or above the upper limits of modern plate velocities and are far higher than global erosion rates (e.g. Larson *et al.*, 1997; Montgomery & Brandon, 2002). Rates would need to be even higher as retrogression reduces the maximum timescale.

Although the relatively short duration of eclogite facies conditions is incompatible with typical regional metamorphic *P–T–t* paths, it is consistent with transient heating (temperature increase) via, for example, shear heating, exothermic metamorphic reactions, and/or fluid or melt advection (e.g. Jamtveit *et al.*, 1990, 2021; Camacho *et al.*, 2005; Ague & Baxter, 2007; Chu *et al.*, 2017). Such mechanisms can readily generate local temperature increases of 50–100 °C or more (e.g. Jamtveit *et al.*, 1990; Chu *et al.*, 2017); more extreme values >300 °C have also been postulated (Camacho *et al.*, 2005). Colder surrounding rock can then quench local thermal anomalies and associated diffusion in garnet on timescales of thousands of years or less (e.g. Chu *et al.*, 2017). Thus, if the granulite was at cooler ambient temperatures and the shear zones and other conduits were heated transiently to eclogite facies conditions as proposed by Camacho *et al.* (2005), the total duration of metamorphic activity could have been considerably longer than c. 300 kyr as the eclogite facies diffusion timescale would be part of a more protracted overall metamorphic history.

The measured diffusional relaxation is mainly the result of diffusion that happened during each individual eclogite facies pulse plus whatever additional diffusion occurred at cooler conditions between each pulse. For a simple example, let us assume that the rocks were at an ambient temperature of 600 °C at eclogite facies pressures (1.5–2.2 GPa). The observed garnet diffusion would then represent c. 3–6 Myr. If Holsnøy was at cooler ambient temperatures and underwent multiple 50–100 °C transient heating pulses each followed by rapid cooling, then episodic eclogite facies metamorphic activity may have spanned several million years. This could have provided sufficient time for subduction and exhumation at more reasonable tectonic rates. It is entirely possible that the eclogite facies thermal pulses were extremely short (e.g. Bjørnerud *et al.*, 2002), and that a large fraction of the observed diffusional relaxation actually occurred between the pulses at lower grade conditions.

Transient thermal behavior is consistent with the high surface area, disequilibrium textures preserved in the eclogite facies assemblages that would presumably have attained greater textural equilibrium if at ~700 °C for millions of years. It is also supported by previous studies on the rates and timings of eclogitization. The model of Bjørnerud *et al.* (2002) predicts that regional eclogitization occurred in tens of thousands of years. More recent models of shear zone formation and hydrogen diffusion have suggested that they may have even formed in a matter of years or less (e.g. Kaatz *et al.*, 2022, 2023; Bras *et al.*, 2023). If transient heating only occurred during active eclogitization, this would be consistent with a longer overall timescale of metamorphism ($>10^6$ yr). Consistently, recent zircon geochronology places amphibolite and eclogite facies conditions as penecontemporaneous within age–date uncertainty (e.g. Jamtveit *et al.*, 2018*b*, 2019, 2021). The overlap of ages spanning several million years could

be a result of transient eclogite facies events superimposed on longer duration (>10^6 yr) lower grade conditions as discussed above.

Importantly, if peak eclogite facies temperature conditions were short lived, care must be taken regarding how these conditions are interpreted tectonically and how they are used to inform our understanding of continental subduction processes. The diffusion chronometry results reveal that transient, pulsed events may exert primary controls on the mineralogical, rheological, and geochemical development of subducted lithologies (e.g. Bjørnerud *et al.*, 2002; Camacho *et al.*, 2005; John *et al.*, 2012; Chu *et al.*, 2017; Taetz *et al.*, 2018; Tian *et al.*, 2018). Much work remains to assess the impact of short-lived events on long-term subduction zone processes.

We speculate that there is a connection between the fluid pulses identified herein and transient heating events. If so, there would have been at least two large-scale heating events (Fig. 16b). However, the fluxes required for direct heating via fluid flow down regional temperature gradients (e.g. Camacho *et al.*, 2005) are prohibitively large (e.g. Bickle & McKenzie, 1987; Bjørnerud & Austrheim, 2006). Moreover, such large fluxes would be expected to produce considerable major element metasomatism (e.g. Philpotts & Ague, 2022), but to our knowledge this is not observed (e.g. Jamtveit *et al.*, 1990). We consider it more feasible that the fluid enabled heating via exothermic hydration reactions or frictional shear heating (e.g. Jamtveit *et al.*, 1990, 2021; Camacho *et al.*, 2005).

Localized mechanisms such as shear heating could produce variations in the maximum temperatures attained by shear zones. However, peak temperature conditions of ~700 °C are consistently reported (e.g. Jamtveit *et al.*, 1990; Erambert & Austrheim, 1993; Raimbourg *et al.*, 2007*a*; Bhowany *et al.*, 2018). This could be due, at least in part, to thermal buffering via partial melting (e.g. Schorn *et al.*, 2018). The wet solidus for the Holsnøy eclogite facies assemblages is ~700 °C (Jamtveit *et al.*, 1990), and once melting began, excess thermal energy may have taken the form of latent heat. Furthermore, hot fluid or melt may have then locally transported heat by advection within the eclogite facies shear zones and fractures, creating greater uniformity of temperature. Nonetheless, it is also possible that there was variability in peak temperature conditions across Holsnøy; this remains as an important topic for future study.

Our results are qualitatively consistent with several important tenets of the cold-crust model of Camacho *et al.* (2005), namely that pulsed heating to eclogite facies conditions, mediated at least in part by fluid infiltration, was superimposed on a longer overall metamorphic timescale of >10^6 yr. However, the maximum timescale we obtain for eclogite facies conditions (c. 300 kyr) is over an order of magnitude longer than the ~18-kyr maximum duration that they calculate based on $^{40}Ar/^{39}Ar$ diffusion systematics. Their interpretation also requires Ar-rich, H_2O-poor fluids, very cold ambient temperatures in the blueschist facies (<400 °C; Holsnøy lacks glaucophane), and extreme (>300 °C) heating pulses. We consider these aspects to be physically difficult to achieve and inconsistent with field observations (e.g. Bjørnerud & Austrheim, 2006). In addition, the cold-crust model requires that essentially all diffusion occurred during the transient heating pulses, whereas in our case considerable diffusion was also possible and indeed probable during the time intervals between the pulses. We argue that the ~18-kyr timescale is too short and the temperature range is too large because ^{40}Ar diffusion in phlogopite is likely orders of magnitude slower than previously thought (Nteme *et al.*, 2024). Nonetheless, our models are in agreement regarding the thermally pulsed nature of the eclogite facies metamorphism.

At least some of the compression and decompression may have resulted from non-lithostatic pressure variations through processes such as stress concentration via rheological contrast, reaction volume change, or melt-induced overpressure (e.g. Jamtveit *et al.*, 2009; Vrijmoed *et al.*, 2009; Moulas *et al.*, 2014; Chu *et al.*, 2017; Hess & Ague, 2021). Recent geochronology, petrological evidence, and thermodynamic and thermomechanical modeling suggest that large non-lithostatic pressure variations of several hundred MPa or more may have been integral to the metamorphic history (e.g. Jamtveit *et al.*, 2000, 2018*b*, 2019; Putnis *et al.*, 2021; Zhong *et al.*, 2021; Moulas *et al.*, 2022; Bras *et al.*, 2023; Hess & Ague, 2024*b*). However, models of non-lithostatic pressure require further exploration and comparison with field relationships. Non-lithostatic pressures should vary considerably at the outcrop scale based on factors such as differential stress magnitude, shear zone geometry, and rheology (e.g. Jamtveit *et al.*, 2018*b*; Moulas *et al.*, 2022), and much work remains to document such relationships. Ultimately, regardless of whether some of the pressure variations were due to non-lithostatic processes, the necessity of rapid cooling rates requires localized thermal excursions (Fig. S2). As a result, the short characteristic eclogite facies timescale (c. 300 kyr) is mostly a consequence of the thermal evolution of the terrane.

Finally, the postulated transient heating scenario is inconsistent with slow cooling from 680 °C to amphibolite facies conditions of ~600 °C over 10–15 Myr, as has been inferred from geochronology (e.g. Glodny *et al.*, 2008; Bhowany *et al.*, 2018; Jamtveit *et al.*, 2021). Significantly more diffusion would be recorded by the garnets if cooling was this slow. Instead, it is possible that the age–date results determined by Glodny *et al.* (2008) for amphibolite facies retrograde conditions represent a late, transient heating event (or events) like those that occurred in the eclogite facies.

Compositional stress in mineral replacement reactions

The model differential stresses arising from Ca–Mg–Fe interdiffusion are as large as 400 MPa (e.g. Fig. 13a). Intracrystalline stresses of this magnitude could drive ductile deformation and/or trigger brittle failure (e.g. Karato *et al.*, 1995; Wang & Ji, 1999; Zhang & Green, 2007; Rogowitz *et al.*, 2023). The model stress values are consistent with experimental studies documenting diffusion-induced fracturing of alkali feldspars requiring 300–350 MPa of compositional stress (Neusser *et al.*, 2012; Scheidl *et al.*, 2014).

Our model predicts limited plastic deformation, and consistently, we observe no evidence of significant ductility given the extremely sharp core–rim chemical contacts and micrometer-scale composition changes (e.g. Figs 9c, 11c, and 13c). Viscous dissipation of stress in garnet will be more likely at higher temperatures (e.g. granulite facies; Wang & Ji, 1999; Hess & Ague, 2024*a*). Instead, the chemical maps suggest that the large compositional stresses triggered brittle failure. High-Ca microfractures radiate from the contacts between eclogite and granulite facies garnet into the garnet cores (Fig. 2c, e–g). The microfractures are always oriented at a high angle to the compositional contacts, which is consistent with Mode 1 fracturing resulting from stress developing parallel to the core–rim contacts (Irwin, 1957) as expected with compositional stress. These microfractures cannot be explained solely by tectonic shear stress as they always form at a high angle to the core–rim contacts, irrespective of shear direction (Fig. 18). Their orientation,

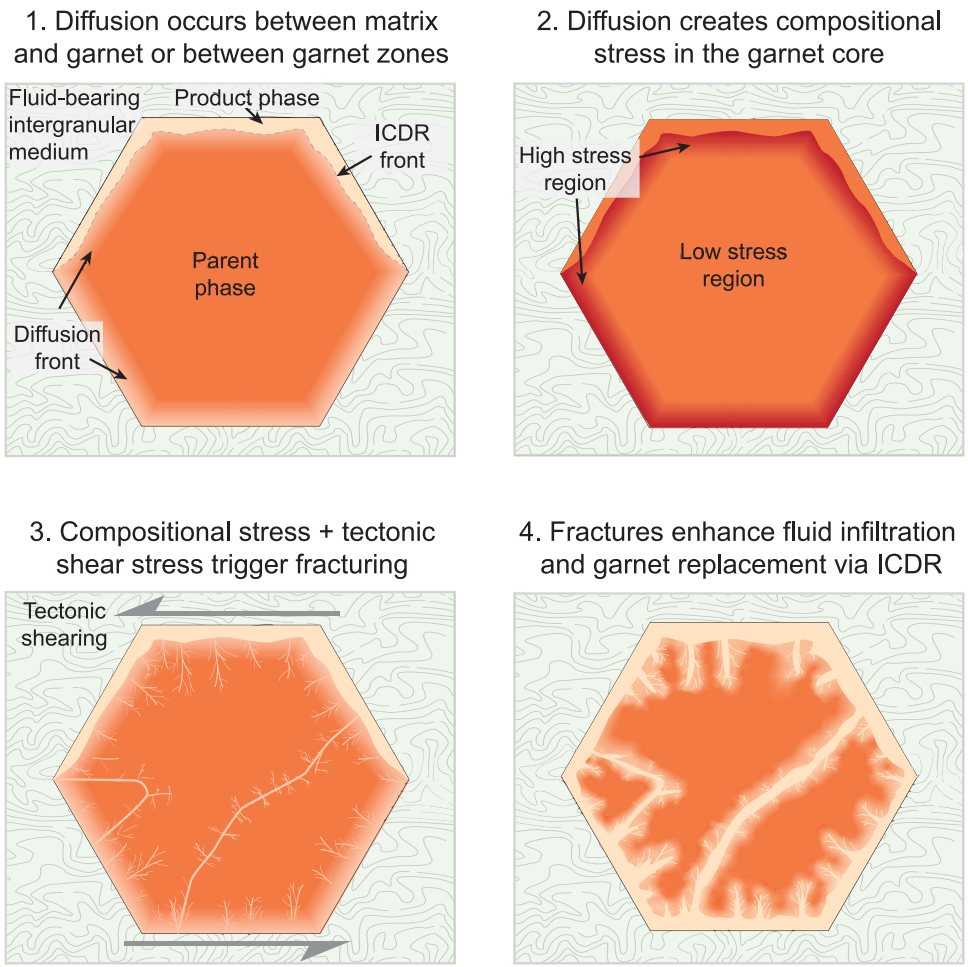

Fig. 18. Feedback between diffusion, compositional stress, and ICDR. (1) Diffusion occurs between the matrix and garnet or between garnet zones. (2) Diffusion creates compositional stress in the garnet interior at the micrometer scale. (3) Compositional stress and shear stress trigger fracturing. (4) Fractures facilitate further diffusion or fluid infiltration and ICDR that continues the feedback loop.

rather, is consistent with the local direction of diffusion and the corresponding predicted stress orientations and magnitudes.

Although brittle failure may partially relieve internal stresses, fractures also provide fast diffusion pathways that increase the flux of Ca into the garnets. Elevated flux of Ca ions into garnet cores would quickly create additional, oscillating intracrystalline stresses that could trigger further fracturing (e.g. Petrishcheva *et al.*, 2019).

Therefore, diffusion-induced stress and fracturing may drive a feedback mechanism wherein diffusion generates stresses that trigger fracturing, allowing for more rapid diffusion into the mineral interior, creating more stress and fracturing (Fig. 18; Neusser *et al.*, 2012; Petrishcheva *et al.*, 2019). This feedback likely operated along the larger eclogite facies fractures that crosscut the garnet cores (e.g. Fig. 2c, e–f).

Fluid may have further contributed to this feedback mechanism through ICDR reactions. The microfractures would create porosity, allowing for more rapid fluid infiltration and ICDR. Diffusion in advance of the newly formed core–rim contacts would generate more compositional stress, continuing the feedback (Fig. 18d). The involvement of fluid is consistent with the observation that the microfractures only propagate from the core–rim boundary into the core. This suggests that the microfractures were contemporaneous and thus coupled with ICDR (Fig. 2a, c, g). Had the microfractures formed later, they would crosscut both core and rim.

Thus, diffusion-induced microfracturing appears to have significantly enhanced garnet replacement reactions on Holsnøy and may be a mechanism that is important in a variety of high-temperature lithospheric settings (Fig. 18; Neusser *et al.*, 2012; Petrishcheva *et al.*, 2019; Beyer & Chakraborty, 2021).

SUMMARY AND CONCLUSIONS

Interdiffusion between different-sized cations in garnet generates intracrystalline, compositional stress that affects garnet's chemical evolution. For peak pressure eclogite facies conditions on Holsnøy (680 °C and 2.1 GPa), standard diffusion models indicate inconsistent metamorphic timescales of 280–320 kyr based on the relatively smooth Alm and Prp zonation and of 1–29 kyr based on sharp Grs features within the same profiles (Fig. 16a). When we incorporate diffusion-induced compositional stress, the sharp Grs contacts are preserved at the longer timescales indicated by Alm and Prp.

Thus, seemingly contradictory observations in fact record a consistent c. 300-kyr timescale (Fig. 16a). This timescale is the maximum duration of eclogite facies conditions as temperature varied little during eclogite facies metamorphism (Bhowany *et al.*, 2018). The timescale could represent either: (1) continuous regional metamorphism or (2) transient heating episodes superimposed on a considerably longer overall metamorphic history. In the first case, the 300-kyr timescale combined with

previously determined stages of eclogite facies compression and decompression (Bhowany *et al.*, 2018) requires extremely rapid regional cooling rates (>2000 °C/Myr) and subduction and exhumation rates of 12 cm/yr or more. These extremely high rates are problematic for conventional plate-driven processes.

Therefore, our results suggest the second model involving transient heating to eclogite facies temperatures (e.g. Jamtveit *et al.*, 1990, 2021; Camacho *et al.*, 2005). This could potentially have included non-lithostatic pressure variations as well (e.g. Jamtveit *et al.*, 2000, 2018*b*, 2019; Putnis *et al.*, 2021; Zhong *et al.*, 2021; Bras *et al.*, 2023; Hess & Ague, 2024*b*). In particular, transient heating events superimposed on, and quenched by, cooler ambient conditions can explain the relatively short duration of eclogite facies temperatures yet still be consistent with a longer overall metamorphic timescale (Camacho *et al.*, 2005). Brief eclogite facies thermal pulses of 50–100 °C (e.g. Jamtveit *et al.*, 1990) lasting cumulatively for much less than the c. 300 kyr maximum timescale (e.g. Bjørnerud *et al.*, 2002), suggest a total metamorphic timescale of $>10^6$ yr. Stated another way, this total is the sum of the pulses plus the intervening periods between the pulses. A timescale of $>10^6$ yr is more compatible with plate-driven subduction and exhumation processes. Short-lived thermal excursions, however, also imply that great care must be taken in making tectonic interpretations from peak temperature conditions. Nonetheless, although they are brief in nature, pulsed events may play a key role in the development of subducted lithologies.

The dry, metastable granulite offered an ideal setting for preserving records of fluid flow via reactions. Eclogite facies garnet rims were formed through ICDR replacement reactions (Pollok *et al.*, 2008), and all rims preserve at least two distinct zones (e.g. Fig. 4f). The timing of the formation of the second rim zones relative to the first is consistent across all samples. This suggests that Holsnøy was subject to two major fluid pulses with evidence for additional more local pulses (Fig. 16b). The episodic fluid pulses could be related to seismic release of fluids from underlying metasediments (Fig. 17; e.g. Sibson, 1990; Ague *et al.*, 1998; Miller *et al.*, 2003; Camacho *et al.*, 2005; Austrheim, 2013; Miller, 2013; Jamtveit *et al.*, 2021). The transient heating events indicated by our timescale results were possibly coupled to the fluid pulses recorded by ICDR (Fig. 16b). If so, the fluids could have enabled heating by triggering exothermic hydration reactions or reactive weakening and shearing (e.g. Jamtveit *et al.*, 1990, 2021; Camacho *et al.*, 2005). In addition, any fluids that were heated by such processes and continued to flow potentially transported heat by local advection within the shear zones.

Finally, we find a coupling between solid-state diffusion, deformation, and ICDR reactions that could be an important driver for mineral replacement reactions in subduction zones and other settings (Fig. 18). Diffusion-induced compositional stress can create a stressed layer around the exterior of minerals such as garnet that triggers fracturing (Fig. 18a–c; e.g. Neusser *et al.*, 2012; Scheidl *et al.*, 2014). The fracture networks provide fast pathways for vacancy-mediated diffusion and create porosity to facilitate ICDR reactions (Fig. 18d). Continued diffusion ahead of the microfractures or the ICDR replacement front creates further compositional stress that forms and propagates additional microfractures (e.g. Petrishcheva *et al.*, 2019). This process creates a feedback mechanism by which both intracrystalline diffusion and fluid can more effectively replace mineral phases.

Ultimately, garnet from Holsnøy provides a consistent metamorphic history when the concurrent, underlying processes of diffusion, intracrystalline stress generation, fracturing, and ICDR are combined. A fully integrated treatment of these processes is required to obtain the robust temporal constraints necessary for testing tectonometamorphic models.

SUPPLEMENTARY DATA

Supplementary data are available at *Journal of Petrology* online.

ACKNOWLEDGEMENTS

We thank A.A. Haws, D.S. Keller, N. Norbraten, and S. Piazolo for thoughtful discussions, and J.O. Eckert, Jr., for valuable assistance with the EPMA. We are particularly grateful to A. Putnis and C.V. Putnis for introducing us to their landmark work on interface-coupled dissolution–reprecipitation. Finally, we greatly appreciate the critical reviews of K. Pollok and A.J. Smye and the editorial handling of J. Hermann, all of which improved our study. This work was supported by the US National Science Foundation Directorate of Geosciences [EAR-2208229] and Yale University.

DATA AVAILABILITY

All data supporting the findings of this work are provided in the manuscript or in the Supplementary Information files and are also stored in a permanent DOI repository (GFZ Data Services) (Hess *et al.*, 2025*a*; doi:https://doi.org/10.5880/fidgeo.2025.017). The codes used to generate the model results presented in this work are available from a permanent DOI repository (Zenodo) (Hess *et al.*, 2025*b*; doi:https://doi.org/10.5281/zenodo.14983229).

REFERENCES

Abart, R., Petrishcheva, E., Habler, G., Sutter, C., Fischer, F. D., Predan, J., Kegl, M. & Rammerstorfer, F. G. (2022). Evolution of chemically induced cracks in alkali feldspar: thermodynamic analysis. *Physics and Chemistry of Minerals* **49**(5), 14. https://doi.org/10.1007/s00269-022-01183-9.

Adegoke, I. A., Xia, F., Deditius, A. P., Pearce, M. A., Roberts, M. P. & Brugger, J. (2022). A new mode of mineral replacement reactions involving the synergy between fluid-induced solid-state diffusion and dissolution-reprecipitation: a case study of the replacement of bornite by copper sulfides. *Geochimica et Cosmochimica Acta* **330**, 165–190. https://doi.org/10.1016/j.gca.2021.04.017.

Ague, J. J. & Axler, J. A. (2016). Interface coupled dissolution-reprecipitation in garnet from subducted granulites and ultrahigh-pressure rocks revealed by phosphorous, sodium, and titanium zonation. *American Mineralogist* **101**(7), 1696–1699. https://doi.org/10.2138/am-2016-5707.

Ague, J. J. & Baxter, E. F. (2007). Brief thermal pulses during mountain building recorded by Sr diffusion in apatite and multicomponent diffusion in garnet. *Earth and Planetary Science Letters* **261**(3–4), 500–516. https://doi.org/10.1016/j.epsl.2007.07.017.

Ague, J. J. & Carlson, W. D. (2013). Metamorphism as garnet sees it: the kinetics of nucleation and growth, equilibration, and diffusional relaxation. *Elements* **9**(6), 439–445. https://doi.org/10.2113/gselements.9.6.439.

Ague, J. J., Park, J. & Rye, D. M. (1998). Regional metamorphic dehydration and seismic hazard. *Geophysical Research Letters* **25**(22), 4221–4224. https://doi.org/10.1029/1998GL900124.

Ague, J. J., Eckert, J. O. & Jr. (2012). Precipitation of rutile and ilmenite needles in garnet: implications for extreme metamorphic conditions in the Acadian Orogen, USA. *American Mineralogist* **97**(5–6), 840–855. https://doi.org/10.2138/am.2012.4015.

Altree-Williams, A., Pring, A., Ngothai, Y. & Brugger, J. (2015). Textural and compositional complexities resulting from coupled dissolution–reprecipitation reactions in geomaterials. *Earth-Science Reviews* **150**, 628–651. https://doi.org/10.1016/j.earscirev.2015.08.013.

Andersen, T., Austrheim, H. & Burke, E. A. J. (1990). Fluid inclusions in granulites and eclogites from the Bergen Arcs, Caledonides of W. Norway. *Mineralogical Magazine* **54**(375), 145–158. https://doi.org/10.1180/minmag.1990.054.375.02.

Austrheim, H. (1987). Eclogitization of lower crustal granulites by fluid migration through shear zones. *Earth and Planetary Science Letters* **81**(2–3), 221–232. https://doi.org/10.1016/0012-821X(87)90158-0.

Austrheim, H. (2013). Fluid and deformation induced metamorphic processes around Moho beneath continent collision zones: examples from the exposed root zone of the Caledonian mountain belt, W-Norway. *Tectonophysics* **609**, 620–635. https://doi.org/10.1016/j.tecto.2013.08.030.

Austrheim, H. & Griffin, W. L. (1985). Shear deformation and eclogite formation within granulite-facies anorthosites of the Bergen Arcs, western Norway. *Chemical Geology* **50**(1–3), 267–281. https://doi.org/10.1016/0009-2541(85)90124-X.

Austrheim, H., Erambert, M. & Engvik, A. K. (1997). Processing of crust in the root of the Caledonian continental collision zone: the role of eclogitization. *Tectonophysics* **273**(1–2), 129–153. https://doi.org/10.1016/S0040-1951(96)00291-0.

Baïsset, M., Labrousse, L., Yamato, P. & Schubnel, A. (2023). Twinning and partial melting as early weakening processes in plagioclase at high pressure: insights from Holsnøy (Scandinavian Caledonides, Norway). *Contributions to Mineralogy and Petrology* **178**(3), 19. https://doi.org/10.1007/s00410-023-01998-x.

Baumgartner, L., Floess, D., Podladchikov, Y. & Foster, C., Jr. (2010) *Pressure Gradients in Garnets Induced by Diffusion Relaxation of Major Element Zoning*. Denver, USA: In Geological Society of America.

Beyer, C. & Chakraborty, S. (2021). Internal stress-induced recrystallization and diffusive transport in $CaTiO_3$-$PbTiO_3$ solid solutions: a new transport mechanism in geomaterials and its implications for thermobarometry, geochronology, and geospeedometry. *American Mineralogist: Journal of Earth and Planetary Materials* **106**(12), 1940–1949. https://doi.org/10.2138/am-2021-7588.

Bhowany, K., Hand, M., Clark, C., Kelsey, D. E., Reddy, S. M., Pearce, M. A., Tucker, N. M. & Morrissey, L. J. (2018). Phase equilibria modelling constraints on P–T conditions during fluid catalysed conversion of granulite to eclogite in the Bergen Arcs, Norway. *Journal of Metamorphic Geology* **36**(3), 315–342.

Bickle, M. J. & McKenzie, D. (1987). The transport of heat and matter by fluids during metamorphism. *Contributions to Mineralogy and Petrology* **95**(3), 384–392. https://doi.org/10.1007/BF00371852.

Bingen, B., Davis, W. J. & Austrheim, H. (2001). Zircon U-Pb geochronology in the Bergen arc eclogites and their Proterozoic protoliths, and implications for the pre-Scandian evolution of the Caledonides in western Norway. *Geological Society of America Bulletin* **113**(5), 640–649. https://doi.org/10.1130/0016-7606(2001)113<0640:ZUPGIT>2.0.CO;2.

Bjørnerud, M. G. & Austrheim, H. (2006). Hot fluids or rock in eclogite metamorphism? *Nature* **440**(7082), E4–E4. https://doi.org/10.1038/nature04714.

Bjørnerud, M. G., Austrheim, H. & Lund, M. G. (2002). Processes leading to eclogitization (densification) of subducted and tectonically buried crust. *Journal of Geophysical Research: Solid Earth* **107**(B10), ETG-14.

Borg, S., Liu, W., Pearce, M., Cleverley, J. & MacRae, C. (2014). Complex mineral zoning patterns caused by ultra-local equilibrium at reaction interfaces. *Geology* **42**(5), 415–418. https://doi.org/10.1130/G35287.1.

Borinski, S. A., Hoppe, U., Chakraborty, S., Ganguly, J. & Bhowmik, S. K. (2012). Multicomponent diffusion in garnets I: general theoretical considerations and experimental data for Fe–Mg systems. *Contributions to Mineralogy and Petrology* **164**, 571–586. https://doi.org/10.1007/s00410-012-0758-0.

Boundy, T. M., Fountain, D. M. & Austrheim, H. (1992). Structural development and petrofabrics of eclogite facies shear zones, Bergen Arcs, western Norway: implications for deep crustal deformational processes. *Journal of Metamorphic Geology* **10**(2), 127–146. https://doi.org/10.1111/j.1525-1314.1992.tb00075.x.

Boundy, T. M., Essene, E. J., Hall, C. M., Austrheim, H. & Halliday, A. N. (1996). Rapid exhumation of lower crust during continent-continent collision and late extension: evidence from 40Ar/39Ar incremental heating of hornblendes and muscovites, Caledonian orogen, western Norway. *Geological Society of America Bulletin* **108**(11), 1425–1437. https://doi.org/10.1130/0016-7606(1996)108<1425:REOLCD>2.3.CO;2.

Boundy, T. M., Mezger, K. & Essene, E. J. (1997). Temporal and tectonic evolution of the granulite-eclogite association from the Bergen Arcs, western Norway. *Lithos* **39**(3–4), 159–178. https://doi.org/10.1016/S0024-4937(96)00026-6.

Boundy, T. M., Donohue, C. L., Essene, E. J., Mezger, K. & Austrheim, H. (2002). Discovery of eclogite facies carbonate rocks from the Lindås Nappe, Caledonides, Western Norway. *Journal of Metamorphic Geology* **20**(7), 649–667. https://doi.org/10.1046/j.1525-1314.2002.00396.x.

Brady, J. B. (1983). Intergranular diffusion in metamorphic rocks. *American Journal of Science* **283**, 181–200.

Bras, E., Baïsset, M., Yamato, P. & Labrousse, L. (2021). Transient weakening during the granulite to eclogite transformation within hydrous shear zones (Holsnøy, Norway). *Tectonophysics* **819**, 229026. https://doi.org/10.1016/j.tecto.2021.229026.

Bras, E., Yamato, P., Schmalholz, S. M., Duretz, T. & Podladchikov, Y. Y. (2023). Eclogitisation of dry and impermeable granulite by fluid flow with reaction-induced porosity: insights from hydrochemical modelling. *Earth and Planetary Science Letters* **617**, 118256. https://doi.org/10.1016/j.epsl.2023.118256.

Caddick, M. J., Konopásek, J. & Thompson, A. B. (2010). Preservation of garnet growth zoning and the duration of prograde metamorphism. *Journal of Petrology* **51**(11), 2327–2347. https://doi.org/10.1093/petrology/egq059.

Camacho, A., Lee, J. K., Hensen, B. J. & Braun, J. (2005). Short-lived orogenic cycles and the eclogitization of cold crust by spasmodic hot fluids. *Nature* **435**(7046), 1191–1196. https://doi.org/10.1038/nature03643.

Carlson, W. D. (2006). Rates of Fe, Mg, Mn, and Ca diffusion in garnet. *American Mineralogist* **91**(1), 1–11. https://doi.org/10.2138/am.2006.2043.

Centrella, S. (2019). The granulite-to eclogite-and amphibolite-facies transition: a volume and mass transfer study in the Lindås Nappe, Bergen Arcs, West Norway. *Geological Society, London, Special Publications* **478**(1), 241–264. https://doi.org/10.1144/SP478.9.

Centrella, S., Austrheim, H. & Putnis, A. (2015). Coupled mass transfer through a fluid phase and volume preservation during the hydration of granulite: an example from the Bergen Arcs, Norway. *Lithos* **236**, 245–255.

Chakraborty, S. & Ganguly, J. (1992). Cation diffusion in aluminosilicate garnets: experimental determination in spessartine-almandine diffusion couples, evaluation of effective binary diffusion coefficients, and applications. *Contributions to Mineralogy and Petrology* **111**(1), 74–86. https://doi.org/10.1007/BF00296579.

Chaves, E. J. & Schwartz, S. Y. (2016). Monitoring transient changes within overpressured regions of subduction zones using ambient seismic noise. *Science Advances* **2**(1), e1501289. https://doi.org/10.1126/sciadv.1501289.

Chen, J. & Chu, X. (2024). Bridging the gap in garnet diffusion models at low temperatures: recalibration using Western Tianshan eclogitic breccia. *Journal of Petrology* **65**(3), egae012. https://doi.org/10.1093/petrology/egae012.

Chu, X. & Ague, J. J. (2015). Analysis of experimental data on divalent cation diffusion kinetics in aluminosilicate garnets with application to timescales of peak Barrovian metamorphism, Scotland. *Contributions to Mineralogy and Petrology* **170**, 1–27. https://doi.org/10.1007/s00410-015-1175-y.

Chu, X., Ague, J. J., Podladchikov, Y. Y. & Tian, M. (2017). Ultrafast eclogite formation via melting-induced overpressure. *Earth and Planetary Science Letters* **479**, 1–17. https://doi.org/10.1016/j.epsl.2017.09.007.

Crank, J. (1979) *The Mathematics of Diffusion*. Oxford, UK: Oxford University Press.

Dal Zilio, L. & Gerya, T. (2022). Subduction earthquake cycles controlled by episodic fluid pressure cycling. *Lithos* **426**, 106800.

Donohue, C. L. & Essene, E. J. (2000). An oxygen barometer with the assemblage garnet–epidote. *Earth and Planetary Science Letters* **181**(3), 459–472. https://doi.org/10.1016/S0012-821X(00)00219-3.

Engvik, A. K., Putnis, A., Fitz Gerald, J. D. & Austrheim, H. (2008). Albitization of granitic rocks: the mechanism of replacement of oligoclase by albite. *The Canadian Mineralogist* **46**(6), 1401–1415. https://doi.org/10.3749/canmin.46.6.1401.

Engvik, A. K., Golla-Schindler, U., Berndt, J., Austrheim, H. & Putnis, A. (2009). Intragranular replacement of chlorapatite by hydroxy-fluor-apatite during metasomatism. *Lithos* **112**(3–4), 236–246. https://doi.org/10.1016/j.lithos.2009.02.005.

Erambert, M. & Austrheim, H. (1993). The effect of fluid and deformation on zoning and inclusion patterns in poly-metamorphic garnets. *Contributions to Mineralogy and Petrology* **115**(2), 204–214. https://doi.org/10.1007/BF00321220.

Erba, A., Mahmoud, A., Orlando, R. & Dovesi, R. (2014). Elastic properties of six silicate garnet end members from accurate ab initio simulations. *Physics and Chemistry of Minerals* **41**, 151–160. https://doi.org/10.1007/s00269-013-0630-4.

Erdélyi, Z. & Schmitz, G. (2012). Reactive diffusion and stresses in spherical geometry. *Acta Materialia* **60**(4), 1807–1817. https://doi.org/10.1016/j.actamat.2011.12.006.

Faryad, S. W. & Chakraborty, S. (2005). Duration of Eo-Alpine metamorphic events obtained from multicomponent diffusion modeling of garnet: a case study from the eastern Alps. *Contributions to Mineralogy and Petrology* **150**, 306–318. https://doi.org/10.1007/s00410-005-0020-0.

Filiberto, L. H., Austrheim, H., Putnis, A., Padrón-Navarta, J. A., Reddy, S. & Putnis, C. V. (2025). Mechanisms of shear zone development in Krossøy, the Bergen Arcs, Norway. *Lithos* **498-499**, 107977. https://doi.org/10.1016/j.lithos.2025.107977.

Florence, F. P. & Spear, F. S. (1993). Influences of reaction history and chemical diffusion on PT calculations for staurolite schists from the Littleton formation, northwestern New Hampshire. *American Mineralogist* **78**(3–4), 345–359.

Fournelle, J., Cathey, H., Pinard, P. T. & Richter, S. (2016) Low voltage EPMA: experiments on a new frontier in microanalysis-analytical lateral resolution. *IOP Conference Series: Materials Science and Engineering* **109**, 012003.

Ganguly, J., Bhattacharya, R. N. & Chakraborty, S. (1988). Convolution effect in the determination of composition profiles and diffusion coefficients by microprobe step scans. *American Mineralogist* **73**(7–8), 901–909.

Ganguly, J., Cheng, W. & Chakraborty, S. (1998). Cation diffusion in aluminosilicate garnets: experimental determination in pyrope-almandine diffusion couples. *Contributions to Mineralogy and Petrology* **131**, 171–180. https://doi.org/10.1007/s004100050386.

Gardner, R. L., Daczko, N. R., Piazolo, S., Adam, J. & Meek, U. (2025). Melt–rock interaction experiments reveal rapid microstructural and chemical changes at lower crustal conditions. *Journal of Metamorphic Geology* **43**(4), 341–358. https://doi.org/10.1111/jmg.12811.

Geisler, T., Schaltegger, U. & Tomaschek, F. (2007). Re-equilibration of zircon in aqueous fluids and melts. *Elements* **3**(1), 43–50. https://doi.org/10.2113/gselements.3.1.43.

Glodny, J., Kühn, A. & Austrheim, H. (2008). Diffusion versus recrystallization processes in Rb–Sr geochronology: isotopic relics in eclogite facies rocks, Western Gneiss Region, Norway. *Geochimica et Cosmochimica Acta* **72**(2), 506–525. https://doi.org/10.1016/j.gca.2007.10.021.

Griffin, W. L. (1972). Formation of eclogites and the coronas in anorthosites, Bergen Arcs, Norway. *Geological Society of America Memoirs* **135**, 37–64. https://doi.org/10.1130/MEM135-p37.

Hacker, B. R. & Christie, J. M. (1991). Observational evidence for a possible new diffusion path. *Science* **251**(4989), 67–70.

van Haren, J. L. M., Ague, J. J. & Rye, D. M. (1996). Oxygen isotope record of fluid infiltration and mass transfer during regional metamorphism of pelitic schist, south-central Connecticut, USA. *Geochimica et Cosmochimica Acta* **60**, 3487–3504. https://doi.org/10.1016/0016-7037(96)00182-2.

Harlov, D. E., Wirth, R. & Förster, H. J. (2005). An experimental study of dissolution–reprecipitation in fluorapatite: fluid infiltration and the formation of monazite. *Contributions to Mineralogy and Petrology* **150**, 268–286. https://doi.org/10.1007/s00410-005-0017-8.

Harlov, D. E., Wirth, R. & Hetherington, C. J. (2011). Fluid-mediated partial alteration in monazite: the role of coupled dissolution–reprecipitation in element redistribution and mass transfer. *Contributions to Mineralogy and Petrology* **162**, 329–348. https://doi.org/10.1007/s00410-010-0599-7.

Hart, E. W. (1957). On the role of dislocations in bulk diffusion. *Acta Metallurgica* **5**(10), 597. https://doi.org/10.1016/0001-6160(57)90127-X.

Hess, B. L. & Ague, J. J. (2021). Quantifying the effects of non-hydrostatic stress on single-component polymorphs. *Journal of Geophysical Research: Solid Earth* **126**(5), e2020JB021594.

Hess, B. L. & Ague, J. J. (2023). Modeling diffusion in ionic, crystalline solids with internal stress gradients. *Geochimica et Cosmochimica Acta* **354**, 27–37. https://doi.org/10.1016/j.gca.2023.06.004.

Hess, B. L. & Ague, J. J. (2024a). Diffusion-induced stress in crystals: implications for timescales of mountain building. *Lithos* **488**, 107783.

Hess, B. L. & Ague, J. J. (2024b). Orientation piezometry: methods for quantifying stress from the compositions and orientations of multicomponent minerals. *Journal of Geophysical Research: Solid Earth* **129**(12), e2024JB030113.

Hess, B. L., Ague, J. J. & Voorhees, P. W. (2022). Quantifying the effects of non-hydrostatic stress on multi-component minerals. *Journal of Geophysical Research: Solid Earth* **127**(9), e2022JB025201.

Hess, B. L., Ague, J. J. & Austrheim, H. (2025a) *Electron Microprobe Analysis of Garnets from Holsnøy, Norway*. Potsdam, Germany: GFZ Data Services.

Hess, B. L., Ague, J. J. & Austrheim, H. (2025b). Software for modeling coupled diffusion and stress in garnet from Holsnøy, Norway (version 1). *Zenodo.* . https://doi.org/10.5281/zenodo.14983229.

Holland, T. J. B. & Powell, R. (2011). An improved and extended internally consistent thermodynamic dataset for phases of petrological interest, involving a new equation of state for solids. *Journal of Metamorphic Geology* **29**(3), 333–383. https://doi.org/10.1111/j.1525-1314.2010.00923.x.

Irwin, G. R. (1957). Analysis of stresses and strains near the end of a crack traversing a plate. *Journal of Applied Mechanics* **24**, 361–364. https://doi.org/10.1115/1.4011547.

Jamtveit, B., Bucher-Nurminen, K. & Austrheim, H. (1990). Fluid controlled eclogitization of granulites in deep crustal shear zones, Bergen Arcs, Western Norway. *Contributions to Mineralogy and Petrology* **104**, 184–193. https://doi.org/10.1007/BF00306442.

Jamtveit, B., Austrheim, H. & Malthe-Sørenssen, A. (2000). Accelerated hydration of the Earth's deep crust induced by stress perturbations. *Nature* **408**(6808), 75–78. https://doi.org/10.1038/35040537.

Jamtveit, B., Putnis, C. V. & Malthe-Sørenssen, A. (2009). Reaction induced fracturing during replacement processes. *Contributions to Mineralogy and Petrology* **157**, 127–133.

Jamtveit, B., Ben-Zion, Y., Renard, F. & Austrheim, H. (2018a). Earthquake-induced transformation of the lower crust. *Nature* **556**(7702), 487–491. https://doi.org/10.1038/s41586-018-0045-y.

Jamtveit, B., Moulas, E., Andersen, T. B., Austrheim, H., Corfu, F., Petley-Ragan, A. & Schmalholz, S. M. (2018b). High pressure metamorphism caused by fluid induced weakening of deep continental crust. *Scientific Reports* **8**(1), 17011. https://doi.org/10.1038/s41598-018-35200-1.

Jamtveit, B., Petley-Ragan, A., Incel, S., Dunkel, K. G., Aupart, C., Austrheim, H., Corfu, F., Menegon, L. & Renard, F. (2019). The effects of earthquakes and fluids on the metamorphism of the lower continental crust. *Journal of Geophysical Research: Solid Earth* **124**(8), 7725–7755. https://doi.org/10.1029/2018JB016461.

Jamtveit, B., Dunkel, K. G., Petley-Ragan, A., Austrheim, H., Corfu, F. & Schmid, D. W. (2021). Rapid fluid-driven transformation of lower continental crust associated with thrust-induced shear heating. *Lithos* **396**, 106216.

John, T., Gussone, N., Podladchikov, Y. Y., Bebout, G. E., Dohmen, R., Halama, R. & Seitz, H. M. (2012). Volcanic arcs fed by rapid pulsed fluid flow through subducting slabs. *Nature Geoscience* **5**(7), 489–492. https://doi.org/10.1038/ngeo1482.

Jolivet, L., Raimbourg, H., Labrousse, L., Avigad, D., Leroy, Y., Austrheim, H. & Andersen, T. B. (2005). Softening trigerred by eclogitization, the first step toward exhumation during continental subduction. *Earth and Planetary Science Letters* **237**(3–4), 532–547. https://doi.org/10.1016/j.epsl.2005.06.047.

Kaatz, L., Zertani, S., Moulas, E., John, T., Labrousse, L., Schmalholz, S. M. & Andersen, T. B. (2021). Widening of hydrous shear zones during incipient eclogitization of metastable dry and rigid lower crust—Holsnøy, western Norway. *Tectonics* **40**(3), e2020TC006572. https://doi.org/10.1029/2020TC006572.

Kaatz, L., Reynes, J., Hermann, J. & John, T. (2022). How fluid infiltrates dry crustal rocks during progressive eclogitization and shear zone formation: insights from H_2O contents in nominally anhydrous minerals. *Contributions to Mineralogy and Petrology* **177**(7), 72. https://doi.org/10.1007/s00410-022-01938-1.

Kaatz, L., Schmalholz, S. M. & John, T. (2023). Numerical simulations reproduce field observations showing transient weakening during shear zone formation by diffusional hydrogen influx and H_2O inflow. *Geochemistry, Geophysics, Geosystems* **24**(5), e2022GC010830. https://doi.org/10.1029/2022GC010830.

Karato, S. I., Wang, Z., Liu, B. & Fujino, K. (1995). Plastic deformation of garnets: systematics and implications for the rheology of the mantle transition zone. *Earth and Planetary Science Letters* **130**(1–4), 13–30. https://doi.org/10.1016/0012-821X(94)00255-W.

Larché, F. C. & Cahn, J. W. (1982). The effect of self-stress on diffusion in solids. *Acta Metallurgica* **30**(10), 1835–1845. https://doi.org/10.1016/0001-6160(82)90023-2.

Larché, F. C. & Cahn, J. W. (1985). Overview no. 41 the interactions of composition and stress in crystalline solids. *Acta Metallurgica* **33**(3), 331–357. https://doi.org/10.1016/0001-6160(85)90077-X.

Larson, K. M., Freymueller, J. T. & Philipsen, S. (1997). Global plate velocities from the global positioning system. *Journal of Geophysical Research: Solid Earth* **102**(B5), 9961–9981. https://doi.org/10.1029/97JB00514.

Legros, M., Dehm, G., Arzt, E. & Balk, T. J. (2008). Observation of giant diffusivity along dislocation cores. *Science* **319**(5870), 1646–1649. https://doi.org/10.1126/science.1151771.

Love, G. R. (1964). Dislocation pipe diffusion. *Acta Metallurgica* **12**(6), 731–737. https://doi.org/10.1016/0001-6160(64)90220-2.

Mattey, D., Jackson, D. H., Harris, N. B. W. & Kelley, S. (1994). Isotopic constraints on fluid infiltration from an eclogite facies shear zone, Holsenøy, Norway. *Journal of Metamorphic Geology* **12**(3), 311–325. https://doi.org/10.1111/j.1525-1314.1994.tb00025.x.

Miller, S. A. (2013). The role of fluids in tectonic and earthquake processes. *Advances in Geophysics* **54**, 1–46. https://doi.org/10.1016/B978-0-12-380940-7.00001-9.

Miller, S. A., van der Zee, W., Olgaard, D. L. & Connolly, J. A. (2003). A fluid-pressure feedback model of dehydration reactions: experiments, modelling, and application to subduction zones. *Tectonophysics* **370**(1–4), 241–251. https://doi.org/10.1016/S0040-1951(03)00189-6.

Montgomery, D. R. & Brandon, M. T. (2002). Topographic controls on erosion rates in tectonically active mountain ranges. *Earth and Planetary Science Letters* **201**(3–4), 481–489. https://doi.org/10.1016/S0012-821X(02)00725-2.

Moulas, E., Burg, J. P. & Podladchikov, Y. (2014). Stress field associated with elliptical inclusions in a deforming matrix: mathematical model and implications for tectonic overpressure in the lithosphere. *Tectonophysics* **631**, 37–49. https://doi.org/10.1016/j.tecto.2014.05.004.

Moulas, E., Kaus, B. & Jamtveit, B. (2022). Dynamic pressure variations in the lower crust caused by localized fluid-induced weakening. *Communications Earth & Environment* **3**(1), 157. https://doi.org/10.1038/s43247-022-00478-7.

Neusser, G., Abart, R., Fischer, F. D., Harlov, D. & Norberg, N. (2012). Experimental Na/K exchange between alkali feldspar and an NaCl–KCl salt melt: chemically induced fracturing and element partitioning. *Contributions to Mineralogy and Petrology* **164**, 341–358. https://doi.org/10.1007/s00410-012-0741-9.

Nteme, J., Scaillet, S., Brault, P., Tassan-Got, L. & Duval, F. (2024). 40Ar diffusion in phlogopite: PVT atomistic calibration and implications for Ar–melt–solid kinetic interactions and ascent dynamics of mantle xenoliths and kimberlites. *Geochimica et Cosmochimica Acta* **382**, 103–117. https://doi.org/10.1016/j.gca.2024.07.008.

Peillod, A., Hess, B., Moulas, E., Hector, S., Patten, C. G., Beranoaguirre, A. & Ring, U. (2025). Duration of isobaric heating and slab rollback in the Aegean extensional province, eastern Mediterranean: evidence from garnet diffusion modelling. *Earth and Planetary Science Letters* **663**, 119409. https://doi.org/10.1016/j.epsl.2025.119409.

Perchuk, A. L. (2002). Eclogites of the Bergen Arcs complex, Norway: petrology and mineral chronometry. *Petrologiya* **10**(2), 99–118.

Petley-Ragan, A., Dunkel, K. G., Austrheim, H., Ildefonse, B. & Jamtveit, B. (2018). Microstructural records of earthquakes in the lower

crust and associated fluid-driven metamorphism in plagioclase-rich granulites. *Journal of Geophysical Research: Solid Earth* **123**(5), 3729–3746. https://doi.org/10.1029/2017JB015348.

Petrishcheva, E., Rieder, M., Predan, J., Fischer, F. D., Giester, G. & Abart, R. (2019). Diffusion-controlled crack propagation in alkali feldspar. *Physics and Chemistry of Minerals* **46**, 15–26. https://doi.org/10.1007/s00269-018-0983-9.

Philpotts, A. R. & Ague, J. J. (2022) *Principles of Igneous and Metamorphic Petrology*. Cambridge, UK: Cambridge University Press.

Piazolo, S., La Fontaine, A., Trimby, P., Harley, S., Yang, L., Armstrong, R. & Cairney, J. M. (2016). Deformation-induced trace element redistribution in zircon revealed using atom probe tomography. *Nature Communications* **7**(1), 10490.

Plümper, O. & Putnis, A. (2009). The complex hydrothermal history of granitic rocks: multiple feldspar replacement reactions under subsolidus conditions. *Journal of Petrology* **50**(5), 967–987. https://doi.org/10.1093/petrology/egp028.

Pollok, K., Jamtveit, B. & Putnis, A. (2001). Analytical transmission electron microscopy of oscillatory zoned grandite garnets. *Contributions to Mineralogy and Petrology* **141**(3), 358–366. https://doi.org/10.1007/s004100100248.

Pollok, K., Lloyd, G. E., Austrheim, H. & Putnis, A. (2008). Complex replacement patterns in garnets from Bergen Arcs eclogites: a combined EBSD and analytical TEM study. *Geochemistry* **68**(2), 177–191. https://doi.org/10.1016/j.chemer.2007.12.002.

Pollok, K., Putnis, C. V. & Putnis, A. (2011). Mineral replacement reactions in solid solution-aqueous solution systems: volume changes, reactions paths and end-points using the example of model salt systems. *American Journal of Science* **311**(3), 211–236. https://doi.org/10.2475/03.2011.02.

Putnis, A. (2002). Mineral replacement reactions: from macroscopic observations to microscopic mechanisms. *Mineralogical Magazine* **66**(5), 689–708. https://doi.org/10.1180/0026461026650056.

Putnis, A. (2009). Mineral replacement reactions. *Reviews in Mineralogy and Geochemistry* **70**(1), 87–124. https://doi.org/10.2138/rmg.2009.70.3.

Putnis, A. (2021). Fluid–mineral interactions: controlling coupled mechanisms of reaction, mass transfer and deformation. *Journal of Petrology* **62**(12), egab092. https://doi.org/10.1093/petrology/egab092.

Putnis, A. & Austrheim, H. (2010). Fluid-induced processes: metasomatism and metamorphism. *Geofluids* **10**(1–2), 254–269. https://doi.org/10.1111/j.1468-8123.2010.00285.x.

Putnis, A. & John, T. (2010). Replacement processes in the Earth's crust. *Elements* **6**(3), 159–164. https://doi.org/10.2113/gselements.6.3.159.

Putnis, A. & Putnis, C. V. (2007). The mechanism of reequilibration of solids in the presence of a fluid phase. *Journal of Solid State Chemistry* **180**(5), 1783–1786.

Putnis, C. V. & Putnis, A. (2022). A mechanism of ion exchange by interface-coupled dissolution-precipitation in the presence of an aqueous fluid. *Journal of Crystal Growth* **600**, 126840. https://doi.org/10.1016/j.jcrysgro.2022.126840.

Putnis, C. V., Geisler, T., Schmid-Beurmann, P., Stephan, T. & Giampaolo, C. (2007). An experimental study of the replacement of leucite by analcime. *American Mineralogist* **92**(1), 19–26. https://doi.org/10.2138/am.2007.2249.

Putnis, A., Jamtveit, B. & Austrheim, H. (2017). Metamorphic processes and seismicity: the Bergen Arcs as a natural laboratory. *Journal of Petrology* **58**(10), 1871–1898. https://doi.org/10.1093/petrology/egx076.

Putnis, A., Moore, J., Prent, A. M., Beinlich, A. & Austrheim, H. (2021). Preservation of granulite in a partially eclogitized terrane: metastable phenomena or local pressure variations? *Lithos* **400**, 106413.

Raimbourg, H., Jolivet, L., Labrousse, L., Leroy, Y. & Avigad, D. (2005). Kinematics of syneclogite deformation in the Bergen Arcs, Norway: implications for exhumation mechanisms. *Geological Society, London, Special Publications* **243**(1), 175–192. https://doi.org/10.1144/GSL.SP.2005.243.01.13.

Raimbourg, H., Goffé, B. & Jolivet, L. (2007a). Garnet reequilibration and growth in the eclogite facies and geodynamical evolution near peak metamorphic conditions. *Contributions to Mineralogy and Petrology* **153**, 1–28. https://doi.org/10.1007/s00410-006-0130-3.

Raimbourg, H., Jolivet, L. & Leroy, Y. (2007b). Consequences of progressive eclogitization on crustal exhumation, a mechanical study. *Geophysical Journal International* **168**(1), 379–401. https://doi.org/10.1111/j.1365-246X.2006.03130.x.

Renard, F., Røyne, A. & Putnis, C. V. (2019). Timescales of interface-coupled dissolution-precipitation reactions on carbonates. *Geoscience Frontiers* **10**(1), 17–27. https://doi.org/10.1016/j.gsf.2018.02.013.

Rogowitz, A., Thielmann, M., Kraus, K., Grasemann, B. & Renner, J. (2023). The effect of the garnet content on deformation mechanisms and weakening of eclogite: insights from deformation experiments and numerical simulations. *Geochemistry, Geophysics, Geosystems* **24**(3), e2022GC010743. https://doi.org/10.1029/2022GC010743.

Rubatto, D., Muentener, O., Barnhoorn, A. & Gregory, C. (2008). Dissolution-reprecipitation of zircon at low-temperature, high-pressure conditions (Lanzo massif, Italy). *American Mineralogist* **93**(10), 1519–1529. https://doi.org/10.2138/am.2008.2874.

Ruiz-Agudo, E., Putnis, C. V. & Putnis, A. (2014). Coupled dissolution and precipitation at mineral–fluid interfaces. *Chemical Geology* **383**, 132–146. https://doi.org/10.1016/j.chemgeo.2014.06.007.

Scheidl, K. S., Schaeffer, A. K., Petrishcheva, E., Habler, G., Fischer, F. D., Schreuer, J. & Abart, R. (2014). Chemically induced fracturing in alkali feldspar. *Physics and Chemistry of Minerals* **41**, 1–16. https://doi.org/10.1007/s00269-013-0617-1.

Schorn, S., Diener, J. F., Powell, R. & Stüwe, K. (2018). Thermal buffering in the orogenic crust. *Geology* **46**(7), 643–646. https://doi.org/10.1130/G40246.1.

Schwarzenbach, E. M., Zhong, X., Caddick, M. J., Schmalholz, S. M., Menneken, M., Hecht, L. & John, T. (2021). On exhumation velocities of high-pressure units based on insights from chemical zoning in garnet (Tianshan, NW China). *Earth and Planetary Science Letters* **570**, 117065. https://doi.org/10.1016/j.epsl.2021.117065.

Sibson, R. H. (1990). Conditions for fault-valve behaviour. *Geological Society, London, Special Publications* **54**(1), 15–28. https://doi.org/10.1144/GSL.SP.1990.054.01.02.

Stephenson, G. B. (1988). Deformation during interdiffusion. *Acta Metallurgica* **36**(10), 2663–2683. https://doi.org/10.1016/0001-6160(88)90114-9.

Sung, Y. H., Brugger, J., Ciobanu, C. L., Pring, A., Skinner, W. & Nugus, M. (2009). Invisible gold in arsenian pyrite and arsenopyrite from a multistage Archaean gold deposit: Sunrise dam, eastern Goldfields Province, Western Australia. *Mineralium Deposita* **44**, 765–791. https://doi.org/10.1007/s00126-009-0244-4.

Taetz, S., John, T., Bröcker, M., Spandler, C. & Stracke, A. (2018). Fast intraslab fluid-flow events linked to pulses of high pore fluid pressure at the subducted plate interface. *Earth and Planetary Science Letters* **482**, 33–43. https://doi.org/10.1016/j.epsl.2017.10.044.

Tian, M., Ague, J. J., Chu, X., Baxter, E. F., Dragovic, N., Chamberlain, C. P. & Rumble, D., III (2018). The potential for metamorphic

thermal pulses to develop during compaction-driven fluid flow. *Geochemistry, Geophysics, Geosystems* **19**(1), 232–256. https://doi.org/10.1002/2017GC007269.

Tomaschek, F., Kennedy, A. K., Villa, I. M., Lagos, M. & Ballhaus, C. (2003). Zircons from Syros, Cyclades, Greece—recrystallization and mobilization of zircon during high-pressure metamorphism. *Journal of Petrology* **44**(11), 1977–2002. https://doi.org/10.1093/petrology/egg067.

Vielzeuf, D., Baronnet, A., Perchuk, A. L., Laporte, D. & Baker, M. B. (2007). Calcium diffusivity in alumino-silicate garnets: an experimental and ATEM study. *Contributions to Mineralogy and Petrology* **154**, 153–170. https://doi.org/10.1007/s00410-007-0184-x.

Vrijmoed, J. C., Podladchikov, Y. Y., Andersen, T. B. & Hartz, E. H. (2009). An alternative model for ultra-high pressure in the Svartberget Fe-Ti garnet-peridotite, Western Gneiss Region, Norway. *European Journal of Mineralogy* **21**(6), 1119–1133. https://doi.org/10.1127/0935-1221/2009/0021-1985.

Wang, Z. & Ji, S. (1999). Deformation of silicate garnets: brittle-ductile transition and its geological implications. *Canadian Mineralogist* **37**, 525–541.

Warr, L. N. (2021). IMA–CNMNC approved mineral symbols. *Mineralogical Magazine* **85**(3), 291–320. https://doi.org/10.1180/mgm.2021.43.

White, R. W., Powell, R. & Johnson, T. E. (2014). The effect of Mn on mineral stability in metapelites revisited: new a–x relations for manganese-bearing minerals. *Journal of Metamorphic Geology* **32**(8), 809–828. https://doi.org/10.1111/jmg.12095.

Zertani, S., Labrousse, L., John, T., Andersen, T. B. & Tilmann, F. (2019). The interplay of eclogitization and deformation during deep burial of the lower continental crust—a case study from the Bergen Arcs (Western Norway). *Tectonics* **38**(3), 898–915. https://doi.org/10.1029/2018TC005297.

Zertani, S., John, T., Brachmann, C., Vrijmoed, J. C. & Plümper, O. (2022). Reactive fluid flow guided by grain-scale equilibrium reactions during eclogitization of dry crustal rocks. *Contributions to Mineralogy and Petrology* **177**(6), 61. https://doi.org/10.1007/s00410-022-01928-3.

Zhang, J. & Green, H. W. (2007). Experimental investigation of eclogite rheology and its fabrics at high temperature and pressure. *Journal of Metamorphic Geology* **25**(2), 97–115. https://doi.org/10.1111/j.1525-1314.2006.00684.x.

Zhong, X., Vrijmoed, J., Moulas, E. & Tajčmanová, L. (2017). A coupled model for intragranular deformation and chemical diffusion. *Earth and Planetary Science Letters* **474**, 387–396. https://doi.org/10.1016/j.epsl.2017.07.005.

Zhong, X., Andersen, N. H., Dabrowski, M. & Jamtveit, B. (2019). Zircon and quartz inclusions in garnet used for complementary Raman thermobarometry: application to the Holsnøy eclogite, Bergen Arcs, Western Norway. *Contributions to Mineralogy and Petrology* **174**, 1–17. https://doi.org/10.1007/s00410-019-1584-4.

Zhong, X., Petley-Ragan, A. J., Incel, S. H., Dabrowski, M., Andersen, N. H. & Jamtveit, B. (2021). Lower crustal earthquake associated with highly pressurized frictional melts. *Nature Geoscience* **14**(7), 519–525. https://doi.org/10.1038/s41561-021-00760-x.

Journal of Petrology, 2025, **66**, egaf083
https://doi.org/10.1093/petrology/egaf083
Original Manuscript